MANIPULATION-DRIVEN ADAPTATION FOR ENHANCING MOBILE ROBOT EFFICIENCY AND VERSATILITY

A Dissertation
Presented to
The Academic Faculty

By

Raymond Kim

In Partial Fulfillment
of the Requirements for the Degree
Doctor of Philosophy in the
George W. Woodruff School of Mechanical Engineering
Robotics Program

Georgia Institute of Technology

May 2023

MANIPULATION-DRIVEN ADAPTATION FOR ENHANCING MOBILE ROBOT EFFICIENCY AND VERSATILITY

Thesis committee:

Dr. Anirban Mazumdar
Mechanical Engineering
Georgia Institute of Technology

Dr. Jun Ueda
Mechanical Engineering
Georgia Institute of Technology

Dr. Stephen Balakirsky
Institute for Robotics and Intelligent Machines
Georgia Tech Research Institute

Dr. Aaron Young
Mechanical Engineering
Georgia Institute of Technology

Dr. Jonathan Rogers
Aerospace Engineering
Georgia Institute of Technology

Date approved: April 20, 2023

A true genius admits that he/she knows nothing.

Albert Einstein

This work is dedicated to Jesus Christ, who is and always will be, my constant source of support and encouragement.

ACKNOWLEDGMENTS

All praise, honor, and glory to my Lord Jesus Christ for His richest grace and mercy for the accomplishment of this thesis. Without His blessings, this achievement would not have been possible.

Words cannot express my gratitude to my professor, Anirban Mazumdar, for his invaluable patience and feedback. He has taught me how to be and think like an engineer. I also could not have undertaken this journey without my defense committee, who generously provided knowledge and expertise. Additionally, this endeavor would not have been possible without the generous support from the George W. Woodruff School of Mechanical Engineering, which financed my research.

I would like to thank all the DART Lab members who have supported and helped me finish this project. I would like to thank Adam Foris, Samuel Lutes, Zachary Goddard, Aakash Bajpai, Kathryn Bruss, Bharat Kanwar, Kevin Choi, Samuel Deal, Joshua Fernandez, Haley Hilborn, Carlos Carrasquillo, Matthew Burg, Matthew Connelly, Ryan Casey, Trevor Matteson, Divya Iyengar, Mikhail Bagadion, and Joshua Woodford. They kept me going and this work would not have been possible without their support.

Finally, my deepest gratitude to my parents and friends for their constant prayers and unconditional love. Their confidence bolstered my own through the ebb and flow of this work.

Once again, my sincere thanks to all.

- *Raymond Kim*

TABLE OF CONTENTS

LIST OF TABLES

LIST OF FIGURES

SUMMARY

Terrestrial mobile robotics are crucial to a range of missions including planetary exploration, search and rescue, logistics, and national security. Many of these missions require the robot to operate on a broad variety of terrain. Physical adaptation can enable a robot to intelligently interact with the environment to benefit from efficient and versatile performance. We describe a new approach to physical adaptation through manipulation. Specifically, this work investigates how manipulators can be used to change the vehicle's locomotive capabilities or increase vehicle traction. This work presents "swappable propulsors/anchors", which can be easily attached/detached to adapt the vehicle by exploiting geometric features and permanent magnets. A new robot system that uses its manipulator to swap between propulsors/anchors is created. This work experimentally demonstrates and quantifies how this manipulation-driven adaptation method provides a unique combination of energy efficiency and versatility in performance. We describe the design of swappable propulsors/anchors, analyze how to manipulate them and describe how they can be used to improve performance in mobility and payload transport across various surfaces.

CHAPTER 1
INTRODUCTION

1.1 Overview

Mobile robotics can assist in a variety of important missions including search and rescue, planetary exploration, logistics, and environmental monitoring by maneuvering around small entrances, transporting large payloads, and removing personnel from potential risks [1, 2, 3]. However, such missions often involve interacting with diverse and unpaved terrain. Such terrain can feature substantial variations in height, grade, and friction. These varying conditions can cause performance to degrade and can even result in catastrophic failure.

This article proposes a new manipulation-driven adaptation approach for enhancing mobile robot efficiency and versatility on various surfaces. Specifically, we explore how robots can utilize multi-purpose, vehicle-mounted manipulators to modify their method of movement or ability to resist movement for different terrain. We liken this approach to how humans change shoes for different types of terrain. The ability to change shoes enables a broad range of locomotion capabilities. This can enable motion over varying terrain (running shoes and cleats), different modes of locomotion (shoes and roller skates), and even locomotion in fluids (shoes and flippers). To ensure generality, we refer to features that propel the vehicle as "propulsors." Propulsors can include wheels, legs, propellers, whegs [4], or tracks. We refer to features that increase the overall effective coefficient of friction of the system as "anchors." Anchors can increase vehicle traction to allow the pulling of payloads far greater than the robot mass. The use of manipulation enables the swapping of propulsors/anchors on different surfaces. This concept of "swappable propulsors/anchors" enables a broad range of adaptations while taking advantage of specialized tooling for various applications. The proposed solution of this work is outlined in Figure 1.1.

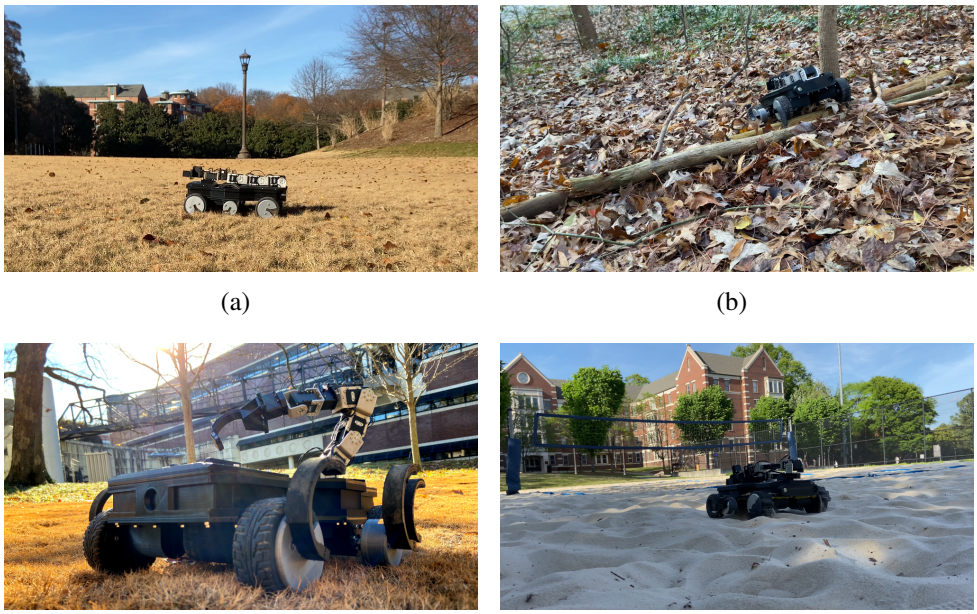

(a) (b) (c) (d)

Figure 1.1: Variations in terrain require mobile robots to physically adapt in order to optimize performance. (a) Wheels are used on flat grounds to enable efficient locomotion. (b) Legs can be used to overcome obstacles. (c) Vehicle-mounted manipulators can enable physical adaptation. (d) A sand propulsor can be devised to physically adapt wheels to prevent slippage.

In this work, we identify key functional requirements to enable simple, yet robust manipulation-based adaptations. Then with these requirements, we present a design framework that can be fashioned to enable adaptive mobility and enhanced payload transport across various surfaces. A unique prototype robot is designed and fabricated to experimentally validate the efficacy of the design. The design, analysis, and experimental evaluation demonstrate that the adaptation method improves energy efficiency and increases the versatility of the system.

This work provides the following key research contributions: 1) developing a new manipulation-based methodology for physical adaptation, 2) creating a permanent-magnet-based mechanical design for swappable propulsors/anchors, 3) experimentally demonstrating that swapping propulsors enable energy efficient and versatile mobility across various surfaces, and 4) experimentally validating that swapping anchors on different surfaces en-

able transportation of loads far greater than the robot mass through the increased effective coefficient of friction.

CHAPTER 2
BACKGROUND AND SIGNIFICANCE

2.1 Terrestrial Mobility

This section outlines some of the current state-of-the-art solutions for terrestrial mobility across various terrain. This article categorizes these solutions into three different categories: static, passive-adaptive, and active-adaptive methods.

2.1.1 Static Methods

The mobile robotics community has produced a plethora of innovative designs for terrestrial locomotion. Currently, many methods rely on static designs that are optimized for specific terrain. Static methods consist of mechanical systems that perform well on a range of surfaces and do not modulate their physical form. Some examples are shown in Figure 2.1. Wheeled robots are common examples of static methods. On relatively flat grounds, wheels maintain continuous contact with the terrain. As a result, wheels are able to travel faster and more efficiently than most legged robots [5]. Wheels are simple and robust in design but are easily obstructed by obstacles greater in height than the radius of the wheel.

Tracks, much like wheels, are also another form of static methods. Specifically, tracks have a much larger surface area of contact than wheels and as a result, they have high traction and exert a much lower pressure on the ground. This feature allows tracks to be an optimal choice on soft, low friction, and uneven ground such as mud, ice, or snow [6, 7]. Although high traction enables versatile locomotion for tracks, it also comes with the drawback of low speed and has the potential to damage paved surfaces.

Whegs or rimless wheels are the practical middle ground between legs and wheels [4]. They combine the simplicity of wheels with discrete contact interactions provided by feet [8].

This morphology allows whegs to change contacts from step to step and traverse varied terrain that cannot be negotiated by wheels of the same radius. However, without articulation in the limbs, whegs inevitably lack critical versatility for contact reconfigurability and are vulnerable to particular substrates such as slatted surfaces or tangled obstacles [9].

Overall, static methods perform well on a range of surfaces but suffer from sub-optimal performance when used in environments that are different from their intended design. As a result, certain terrain can degrade performance or cause complete failure.

(a) (b) (c)

Figure 2.1: Static methods are mechanical systems that perform well on a range of surfaces but do not modulate their physical form. (a) Wheels, (b) tracks, and (c) whegs.

2.1.2 Passive-Adaptive Methods

This problem has led to the growth of adaptive robots. Passive-adaptive systems can adjust their properties without centralized sensing or control. Currently existing solutions are shown in Figure 2.2 and Figure 2.3. This provides increased versatility with relatively low additional complexity. Wheels that can passively alter their radius have been developed for improved versatility [10, 11]. These designs employ a passive mechanism that is triggered by external disturbances from the environment. These methods allow energy-efficient locomotion without any energy input. However, the passive nature of these systems also leads to some drawbacks. First, since adaptation is not controlled, adaptation may occur even when such changes are not desired. Additionally, passive-adaptive systems rely on engineered mechanisms for achieving adaptive behaviors. This can result in additional mass

and mechanical complexity.

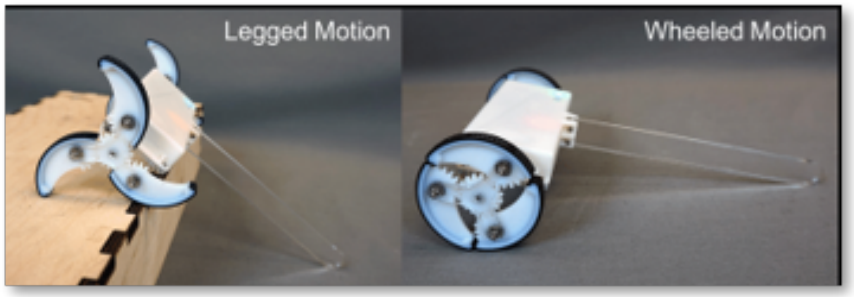

Figure 2.2: Wheel-leg transformers are activated by external triggers such as friction.

Microspines or spring-loaded spines are effective passive-adaptive solutions that can enable mobility on extreme environments such as vertical surfaces through increased traction [12]. These devices perch onto asperities on rough surfaces by distributing the load across numerous millimeter scale spines [13, 14]. The biggest drawback of these designs is that the tips of the spines deteriorate overuse and must be polished or replaced.

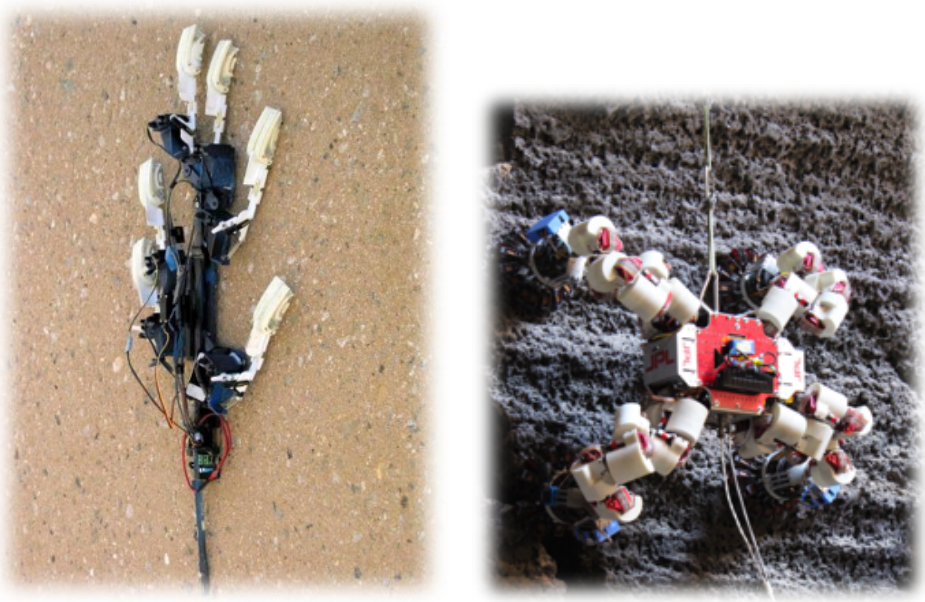

(a) (b)

Figure 2.3: Microspines are effective passive-adaptive solutions that can enable mobility in extreme environments through increased traction. (a) Spinybot II, (b) LEMUR-3.

2.1.3 Active-Adaptive Methods

Active-adaptive methods can provide controlled adaptation. They use energy and actuation to modify their mode of locomotion. Active-adaptive approaches offer increased control. Examples of active-adaptive methods include wheels that can change diameter, deploy spikes [15], or articulate their suspensions, as shown in Figure 2.4. Some designs use controlled deployment of modes based on terrain or even re-positioning of mechanical components to access multi-modal locomotion. Other active-adaptive designs can actively lengthen their spokes to overcome obstacles [16]. One particularly interesting approach is to transition between wheels and legs. Several methods have shown this capability [17, 18]. These are shown in Figure 2.5.

(a) (b)

Figure 2.4: Diameter variable wheels are great examples of active-adaptive methods that use actuation and controls.

Another good example of active-adaptive methods is legs. Legs offer main advantages in applications that require the use of intermittent contacts and the ability to shift the center of mass relative to the contact locations [19]. These advantages chiefly manifest in situations that require both an ability to transverse and manipulate geometrically complex environments through discrete articulation of limbs [20]. In comparison to wheels, legged locomotion offers the most flexibility, versatility, and dexterity in traversing the most difficult terrain [21]. However, in a linear, flat environment, legs are much slower, far less

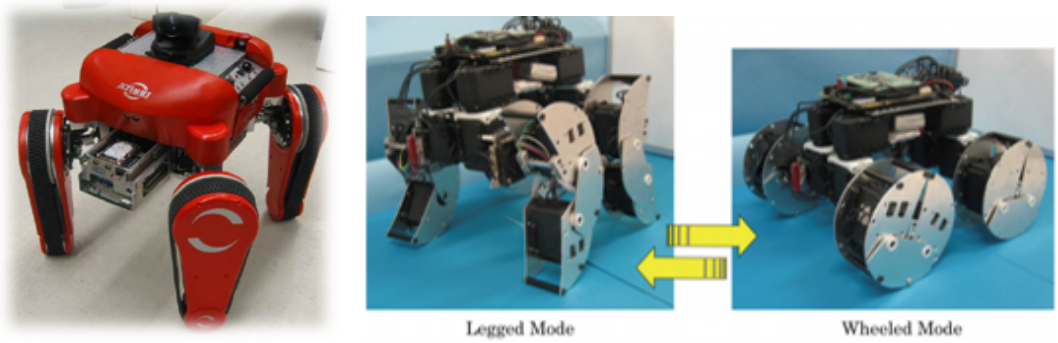

(a) (b)

Figure 2.5: Many transformers that can transition between wheels, legs, or tracks have been developed.

energy efficient, and have limited payload capacity [22].

Active-adaptive designs hold great promise. However, active-adaptive designs feature substantial electrical and mechanical complexity. This includes sensors, actuators, wiring, and electronics. Additionally, incorporating new adaptations can quickly lead to excessive size or weight.

2.2 Payload Transport

Mobile robots can transport large payloads in various environments to improve search and rescue missions and planetary exploration. Outdoor, unstructured, or extra-planet environments often feature diverse terrain with a range of hardness, texture, and wetness. Different surfaces often require unique traction methods. For example, gecko-adhesives perform well on smooth clean surfaces [23] while microspines thrive on hard rough surfaces [13]. In environments with diverse conditions, payload-transport robots must be able to autonomously optimize traction across diverse conditions.

Currently, many innovative solutions exist that increase vehicle traction for payload transport on different types of surfaces. On flat, smooth surfaces, adhesive pads have shown to enable adhesion for mobility and payload transport [24]. Similarly, gecko-inspired adhesives on microbots have demonstrated the ability to pull loads at human scale forces [23,

25]. The overall application of adhesives has been focused on small, microbots and their size entails limited mobility, restricting them to unobstructed, flat, and smooth environments.

On hard, rough surfaces, various solutions have been introduced in the field. Rovers with high-speed vacuum suction modules have been presented to provide high load-carrying capacity [26], but at the cost of significant noise and reduced speed. Legged robots have also been shown to pull heavy payloads on paved asphalt [21], but they require actuation and power to fully engage traction with the given terrain. Microspines are alternate solutions that offer high friction on rough surfaces with asperities. These works demonstrate the benefit of multiple microspines for load sharing and scaling steep, vertical surfaces with high shear forces and little, or even negative, normal forces [12, 13, 27, 28, 29, 30]. Microspines have also been used in applications for gripping and anchoring to increase the overall payload capacity of the system by providing counter-reactionary forces in multiple directions [31, 32]. In particular, leg spines have been shown to improve the performance of millirobots during jumping and pulling on mostly flat or inclined surfaces [33, 34]. Microspines have also been implemented in aerial vehicles to enable perching capabilities for landing and pulling payloads [35, 36]. Other applications include embedded toes to reduce the risk of slip [14]. While microspines have proven to be very effective on rugged terrains with asperities, they also limit the mobility and speed of the system due to their highly adhesive and frictional properties. These robots are designed to perform in extreme environments, and as a result, adaptations to various environments are not preferred.

On soft, granular surfaces, tail-based anchoring robots have been developed to pull heavy payloads by exploiting winch tension and plowing[37]. Mud is also known as a common failure mode for wheeled vehicles, and the literature currently has no clearly optimal solution for traction in mud.

While optimal solutions exist for a range of terrain, such optimal solutions can fail dramatically when used on different terrain. Therefore, there is a need for multi-purpose or

adaptive systems. A recent publication demonstrated a microspine-rubber composite that could be used for multipurpose traction on both smooth and rough surfaces that can support large loads with a high coefficient of friction [38]. In contrast, adaptive solutions can be more complex but offer the potential to provide traction across a larger range of terrain.

2.3 Approach

This work aims to combine the simplicity and robustness of static methods with the controllable versatility of active-adaptive methods. Specifically, this work presents an adaptation solution that utilizes a vehicle-mounted manipulator to physically swap various propulsors/anchors across different surfaces to enhance performance. The remainder of the paper starts by outlining the functional requirements for this new physical adaptation framework. The work then describes the various designs of swappable propulsors which utilize directional magnetic forces for strong attachment and low-force detachment. Finally, a new prototype robot is designed, implemented, and experimentally validated. The experimental results illustrate how such methods can combine both energy efficiency and versatility.

CHAPTER 3

MANIPULATION FOR EFFICIENT AND VERSATILE MOBILITY

3.1 Overall Swappable Propulsor Framework

3.1.1 Functional Requirements

This section outlines general functional requirements that are necessary to achieve the proposed swappable propulsor framework. These requirements are intended to be broadly applicable. Specifically, the propulsor must be able to handle locomotion forces, must be detachable, and must not consume energy when attached. The idea of swappable propulsors can be extended to many types of locomotion, and a few conceptual designs are shown in Figure 3.1. This figure illustrates how propulsors can be designed to traverse flat ground (a), complex terrain (b), soft media (c), or even aquatic environments (d). The presented framework assumes that a mobile robot can store and carry multiple sets of swappable propulsors, each associated with a specific terrain. These propulsors must satisfy certain requirements.

1. ***High holding force when engaged***: During use, the propulsor must remain attached to the robot in the face of the locomotion forces. This can be challenging because the propulsors interact directly with the terrain and can bear a large fraction of the robot's weight.

2. ***Low-force detachment using manipulation***: For the propulsors to be swappable, they must be detachable using a vehicle-mounted manipulator. Vehicle-mounted manipulators have force/weight limitations, so the detachment force should be at least five times less than the minimum holding force.

3. ***Zero power consumption under static conditions***: A key potential advantage of

swappable propulsors is improved energy efficiency. Therefore, swappable propulsor designs should not consume power when engaged or disengaged.

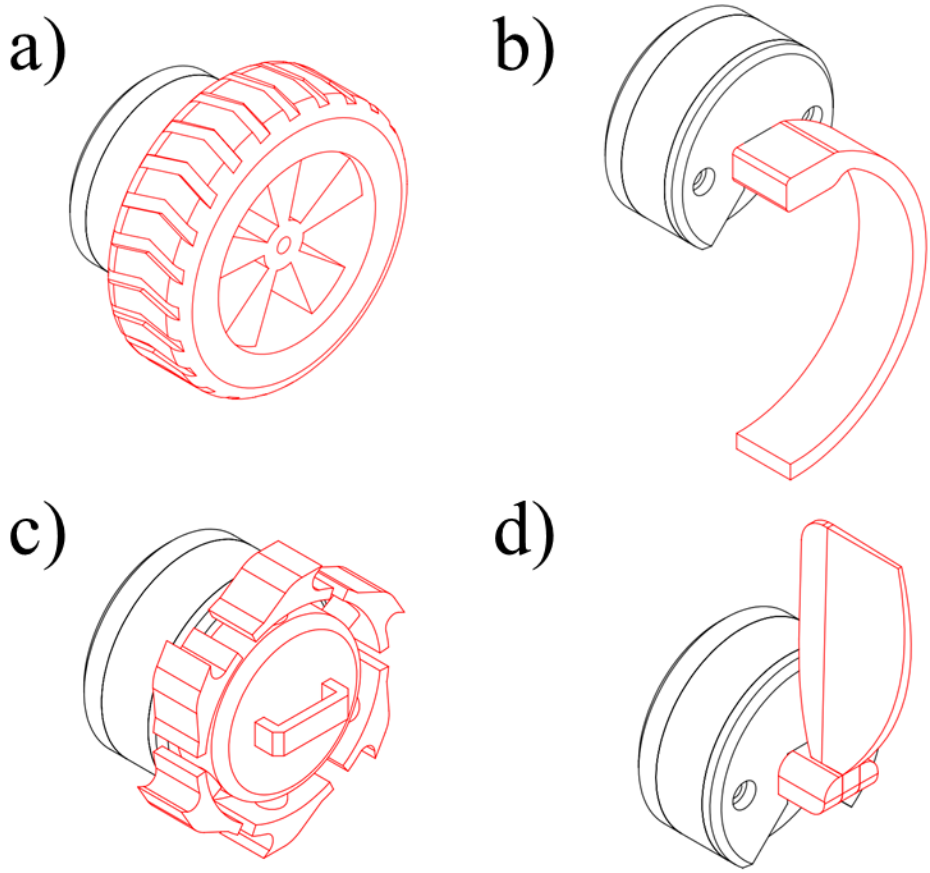

Figure 3.1: a) Swappable wheel propulsor; b) swappable leg propulsor; c) swappable sand propulsor; d) swappable fin propulsor. This figure illustrates the framework of the swappable propulsor. A range of swappable propulsors (red) can be attached to a single housing (black).

3.1.2 Permanent Magnets for Swappable Propulsors

There were no existing methods that satisfied the aforementioned functional requirements. As a result, this work developed a new mounting design for swappable propulsors. This design leverages permanent magnets and mechanical advantage. Permanent magnets enable large attachment forces with low added mass and zero static power consumption. However,

permanent magnets cannot easily be turned on or off. Electromagnets constantly consume power, and electro-permanent magnets require additional coils and electronics [39]. Similarly, internally balanced magnets can have reduced detachment force but would require internal springs and mechanisms for each unit [40].

A simpler solution is to use the manipulator to overcome the magnetic attachment force. If the manipulator is used to pull the propulsor perpendicular to the ferromagnetic surface (y-direction), Figure 3.2 demonstrates that the detachment force F_B would have to be greater than or equal to the magnetic force F_{mag}. This method would require a powerful manipulator that would add considerable mass and complexity to the robot.

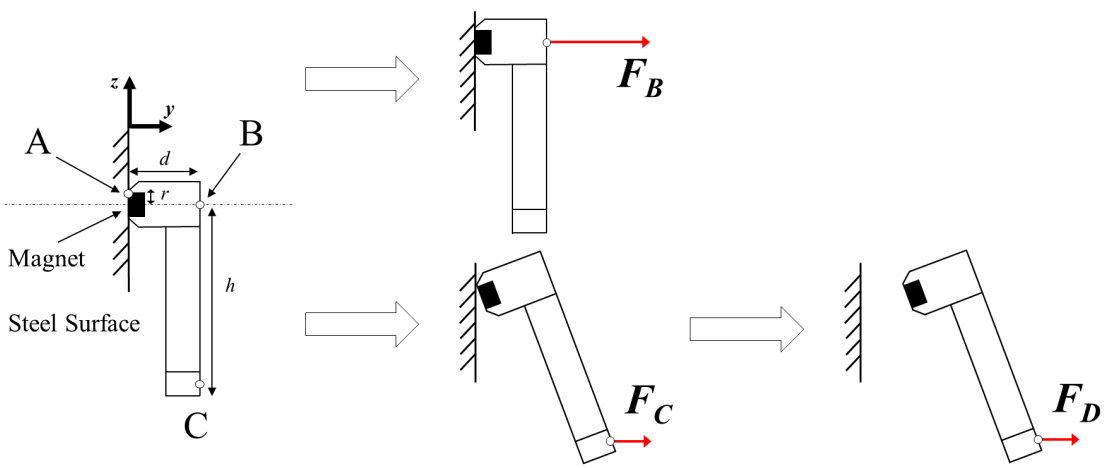

Figure 3.2: Static analysis of the permanent magnet detachment process. Tilting the propulsor can involve less force than pulling against the surface. Once tilted, the propulsor can be easily removed.

Instead of trying to overcome the full magnetic attachment force, the implemented design exploits geometric features. This principle has been used previously for robots moving along steel surfaces [41]. Consider a swappable leg propulsor that has an extrusion with an angled edge so that it can rotate about point A (as shown in Figure 3.2). In this case, r is the distance from the center of the magnet to the angled edge, and the resulting moment created by the magnetic force about point A is $F_{mag}r$.

If a force F_C is applied at the tip of the propulsor (point C) in the positive y-direction, it will produce a moment $F_C h$ about point A. If this moment is greater than $F_{mag}r$, the

propulsor will begin to tilt.

$$F_C > \frac{r}{h} F_{mag} \tag{3.1}$$

As the ratio of h to r becomes larger, the necessary tilting force decreases. In addition, once tilting is initiated, the magnetic attachment force decreases due to the presence of an air gap. The magnet can then be easily detached with a detachment force F_D in the y direction. This approach requires a multi-degree-of-freedom (DoF) manipulator, but can greatly reduce the force/torque requirements.

3.1.3 Mechanically Constraining Steel Surface Mounts

The propulsors see considerable loads during locomotion. They must be able to withstand these loads without detaching or displacing them in an undesired manner. In order to maximize attachment, the design incorporates mating features to augment the magnetic attractive force.

The propulsors are constrained to the robot by steel surface mounts and mechanical frames. The mount consists of a T-slot opening and a surrounding frame. The swappable propulsor has a matching T-slot fitting. The T-slot is used to provide room for attachment and detachment. The T-slot has an angled opening that enables easy attachment and detachment. The framing restricts the magnet-embedded propulsor in every direction except the $-z$ direction (as shown in Figure 3.3). This design is modifiable and is well aligned with ground locomotion where the ground reaction forces would be in the $+z$ direction.

The attachment process, shown in Figure 3.3, consists of placing the swappable propulsor at the T-slot opening with the T-slot fitting aligned with the opening. If the manipulator approaches the T-slot opening within the magnetic attraction force threshold, the embedded magnet will attach itself. Once attached, the propulsor is pushed across the steel surface to the end of the T-slot framing to be constrained.

For detachment, two sequential linear motions are combined. The first motion consists

of a linear drag in the negative z-direction (illustrated in Figure 3.3). The second motion consists of a tilt, followed by a linear pull in the positive y-direction. Once detached,

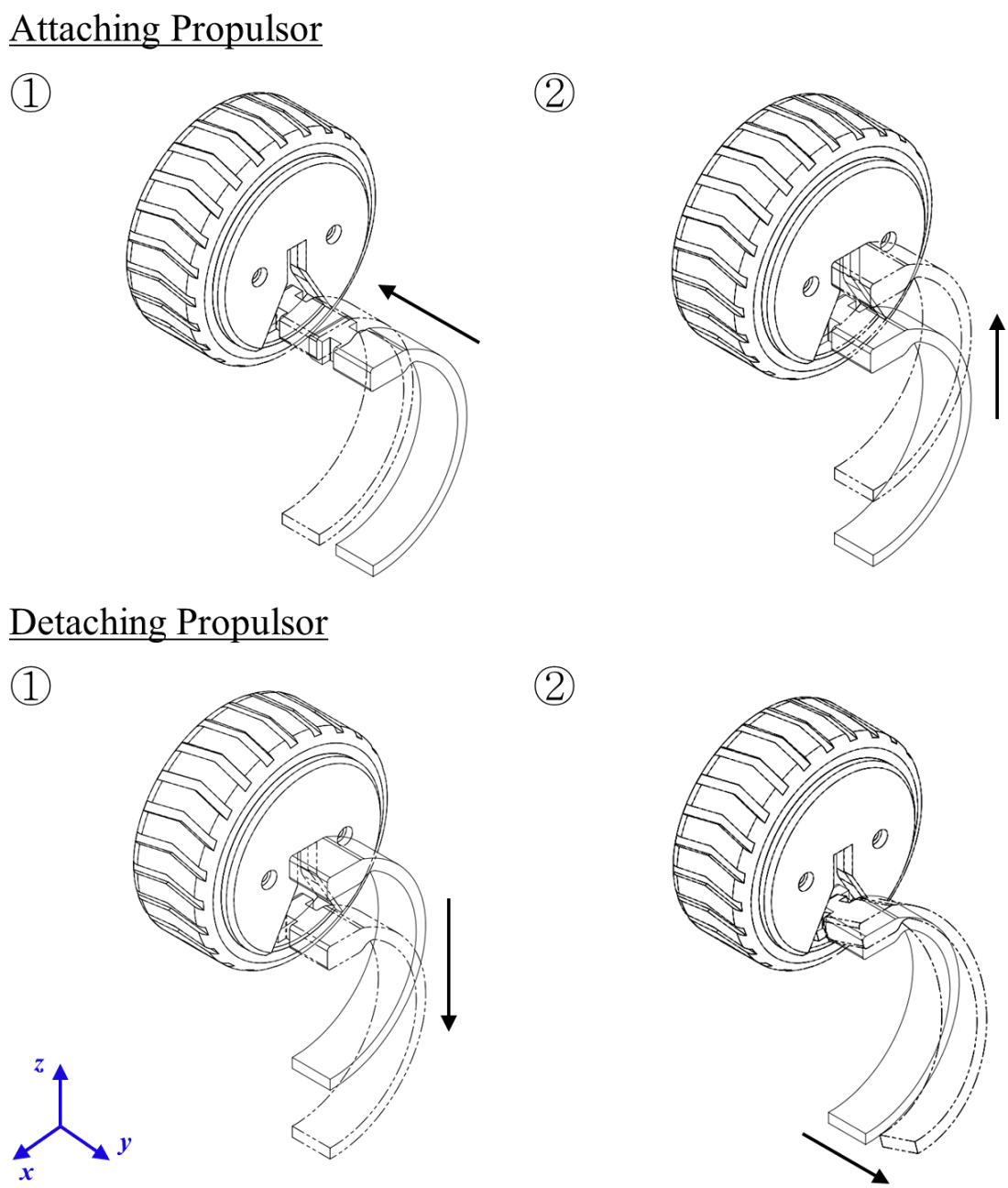

Figure 3.3: Attaching the propulsor requires a two-step motion: 1) the magnet-embedded propulsor attaches to the steel mount once it is brought in proximity; 2) a sliding motion to constrain the T-slot. Detaching the propulsor requires a two-step motion: 1) a sliding motion is required to release the magnet-embedded propulsor from constraint; 2) a lifting motion is required to detach the propulsor.

the propulsors can be stored in the mobile robot. Both the attachment and detachment procedures can be executed using a position-controlled manipulator.

3.2 Vehicle-Mounted Manipulator

Currently, many ground robots carry manipulators to help interact with the environment, deploy sensors, or collect samples. This work is interested in using such multi-DoF manipulators to also attach and detach the swappable propulsors. Specifically, this work considers a 6-DoF serial manipulator with a parallel gripper. The six degrees of freedom were chosen so that the manipulator can reach objects both close and far. Two wrist joints were added so that the feature of the T-slot framing could be properly utilized. The robot arm is illustrated in Figure 3.4.

The arm dimensions are chosen so that the manipulator has the desired workspace. Specifically, the gripper must be able to access both sides of the robot and the storage compartment.

Once the arm dimensions are known (dependent on vehicle size), static analysis can be used to obtain conservative estimates for joint torques during attachment/detachment. Since the manipulator moves relatively slowly during this process, this work assumes that this process is quasi-static. This work primarily focuses on detachment and assumes the forces during attachment are roughly similar. During detachment, the robot arm must impose sufficient forces to first slide the propulsor out of the T-slot, tilt it, and finally pull it off the surface. These force values are typically measured experimentally. The results of this analysis can be used in an approximate manner to a) design the magnetic features based on a known manipulator, or b) select actuators for the manipulator based on the known magnetic and geometric properties. Note, once actuators are identified, the analysis needs to be repeated to account for the gravitational torques caused by the mass of each motor.

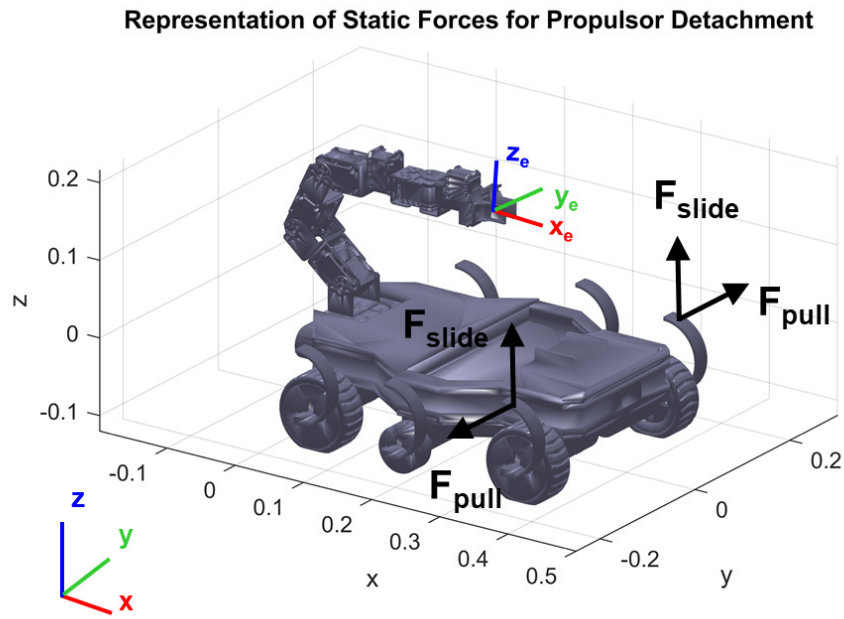

Figure 3.4: A rendering showing the manipulator location, coordinate systems, and detachment force directions relative to the robot.

3.3 Using Adaptation to Improve Performance

When switching between wheels and legs there are two key ways in which adaptation can improve performance. These are 1) energy efficiency, and 2) versatility. Energy efficiency is generally improved if the robot is able to travel using wheels whenever the terrain is traversable. However, if obstacles are present, this creates interesting questions. Often the vehicle can go around the obstacle, but this may take time and waste energy as a result. Therefore, switching to legs may save energy by enabling the robot to take shortcuts. This is only compelling if the energy it takes to swap the propulsors is less than the wasted energy from taking the new path. This work utilizes easily attachable/detachable propulsors and should not require considerable energy. E_{swap} represents the amount of energy used in the swapping process. The swapping energy is the time integral of the arm electrical power,

p_{arm}, and the robot hotel load, p_{hotel}.

$$E_{swap} = \int \left(p_{arm}\left(t\right) + p_{hotel}\left(t\right)\right) dt \tag{3.2}$$

This work assumes that E_{swap} is the same for leg attachment and detachment. For swapping to be energetically valuable, E_{swap} must be less than the difference between the predicted energy with the present configuration and the predicted energy with the adapted configuration.

$$E_{swap} < \int_{0}^{t_{present}} p_{present}\left(t\right) dt - \int_{0}^{t_{adapted}} p_{adapted}\left(t\right) dt \tag{3.3}$$

Note that the time in each mode can be different. This is used to account for the fact that the speed of locomotion is different between modes. More importantly, the path can also vary. For wheels and legs, this trade-off can be thought of as "around the obstacle" or "over the obstacle." Going around using wheels will have low average power consumption, but going over the obstacle with legs may use less total energy.

Switching from wheels to legs can also enable versatility. This is particularly relevant in the presence of obstacles. Wheeled robots have fundamental limits on the size of obstacles they can traverse. Legged robots can often traverse larger obstacles. In some cases, these obstacles may be so prevalent that sustained-legged locomotion is desirable. Other types of swappable propulsors may enable locomotion over insurmountable barriers like steep grades, soft ground, or even water. This versatility not only enables the robot to perform in new environments but also when perception degrades. For example, in cases where obstacle detection is challenging such as rain or night-time, the legged mode could be used due to its superior robustness to terrain.

3.4 Physical Implementation

This section describes the physical implementation of this new approach to adaptive ground mobility. The prototype described in this work is designed to switch between wheels and legs. Each key component is described in detail.

3.4.1 Vehicle Chassis Design

This work utilizes a wheeled vehicle that is capable of either four-wheel drive or six-legged rHex-like locomotion [8]. The vehicle is a relatively flat box with six rotary actuators for locomotion. The wheels are driven by $50 : 1$ metal geared $12V$ DC motors. The wheels are $105mm$ wide. Rubber tires are used on the four wheels. The vehicle frame is made of Polylite PLA and was fabricated using a Lulzbot TAZ 6 FDM style printer. The vehicle prototype is $465mm$ long, $320.8mm$ wide, and $204.8mm$ tall. The vehicle chassis is shown in Figure 3.5. This vehicle is substantially bigger, stronger, and more reliable than the previous prototype.

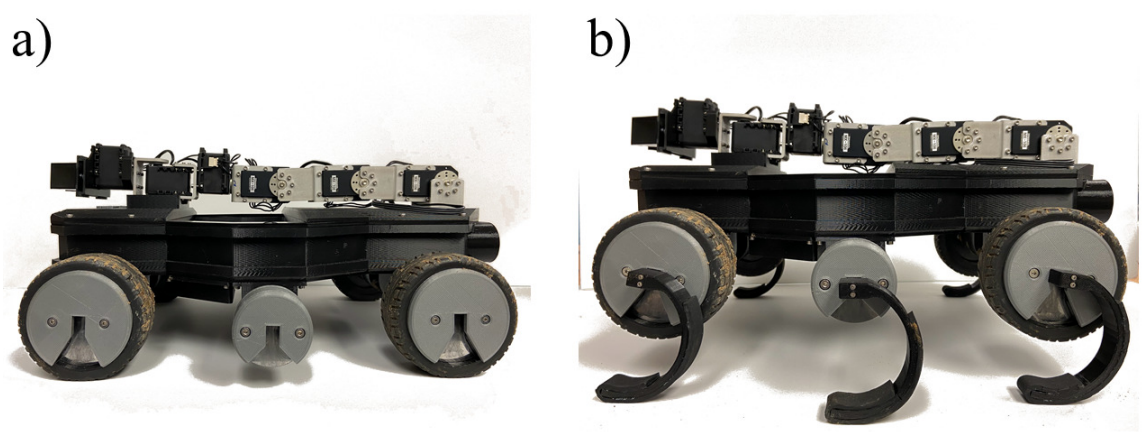

Figure 3.5: a) Wheel mode; b) leg mode. The swappable propulsor prototype has two different modes of locomotion.

3.4.2 Swappable Leg-Wheel Propulsor

The design of the robot is centered around wheeled locomotion. However, the system is designed for easy conversion to legged locomotion. The wheel circumference is covered with a rubber tire, but the interior of the wheel contains the T-slot features described in Section 2. A leg can be added by first servoing the wheel so that the T-slot faces upwards. The leg can then be inserted. The other two motors located in the middle have the T-slot mount but do not have the rubber tire.

The wheels with tires have a diameter of $105mm$, and the legs are based on whegs [8] with a diameter of $100mm$. The T-slots are fabricated using FDM printing. The T-slot mount can withstand up to $56N$. The T-slot opening is covered with a layer of 0.635mm thick 430 stainless steel.

Each magnet is rated for a pull force of $5.4N$. If the manipulator were to detach the propulsor normal to the surface, it would need to exert $9.5N$ of force. The force needed to tilt the propulsor is roughly $0.2N$. Once tilted, the detachment force is greatly reduced and is roughly $0.2N$. It takes roughly $1.8N$ to slide the propulsor on the surface. These forces are measured experimentally.

This means that the robot design can traverse hard terrain using legs because this can lead to primarily high compressive forces (push against the T-slot housing). Traversing softer terrain with legs is more challenging. Terrain that grabs the legs such as leaves or mud can impose tensile (pulling forces). Since these are only resisted by sliding, only $1.8N$ can be tolerated at each foot.

3.4.3 Manipulator Actuator Selection

The force measurements obtained above can be used to acquire rough estimates of the actuator joint torques, τ_J needed for each joint. These estimates can then be used to determine appropriate manipulator actuators. Since the arm actuators are unknown, the arm is assumed to have massless links. The mass of the swappable propulsor is neglected because

it is very small. The measured attachment and detachment forces are combined with the end-effector configuration to predict the necessary joint torques. Note that these torque estimates are low, so actuators need to be sized with a substantial torque margin. These torques are provided in Equation 3.4 with units in Nm.

$$\tau_J \sim \begin{bmatrix} 0.084 & 0.748 & 0.622 & 0.426 & 0.016 & 0.019 \end{bmatrix}^T \tag{3.4}$$

3.4.4 Mobile Manipulator

The maximum torques calculated in Equation 3.4 were used to design the manipulator. Based on the analysis, joints 1, 5, and 6 have relatively low torques. Therefore, these joints were assigned smaller actuators. This helps reduce the size and mass of the manipulator. The manipulator is comprised of three Dynamixel MX-106 servos, two Dynamixel MX-28 servos, and two Dynamixel AX-12A servos. A parallel-jaw gripper driven with an AX-12A servo was designed. The gripper is 3D printed and is rated for a holding force of $4.91N$.

The manipulator is located at the rear of the robot. The manipulator can be used for other purposes beyond swapping propulsors. This can include sampling the environment, manipulating objects, and utilizing sensors. The maximum payload of the manipulator is $400g$. This arm is substantially stronger than the previous prototype in [42].

3.4.5 Modes of Locomotion

The robot utilizes six Pololu metal geared $12V$ DC Motors. The motors have a $50 : 1$ reduction and are capable of $2.1Nm$ extrapolated stall torque and $200RPM$ maximum speed. Each motor has a $64CPR$ encoder. Each motor is controlled with a brushed DC motor controller board.

$Wheel\ Mode$: The wheeled mode of locomotion only uses four of the six motors. The four wheels are regulated using proportional speed control.

$Leg\ Mode$: The leg mode uses all six of the motors coordinated together. A tripod gait

pattern was implemented by using the phase shift gait trajectories in [8, 43]. The position and velocity profiles of the gait pattern were generated and given as inputs for the robot. The trajectories of the legs were tracked with PID position control.

3.4.6 Electronics and Computing

The entire robot system (vehicle and manipulator) is controlled using an Arduino MEGA 2560 microcontroller and an OpenCM9.04 microcontroller expansion board (shown in Figure 3.6). The robot is powered by an 11.1V, 5000 mAh lithium-ion battery. Each locomotion motor is controlled using a motor control board. This board takes in the encoder and hall-effect sensor data and uses a Texas Instruments DRV8871 motor driver to control the motor. Control and communications are performed with an ATMega 328p microcontroller located on each motor control board. The motor controllers communicate with the central microcontroller using I2C. This enables position and velocity control over each of the six motors.

System-level power was measured using an INA260 high-side DC current sensor breakout board. Data was logged to an SD card using the Adafruit Data Logger Shield.

3.5 Experimental Results

3.5.1 Overview

A series of experiments were conducted to evaluate the performance of the robot system. The main objective was to measure the energy consumption and cost of transport on various terrain. Specifically, experiments were performed to evaluate the cost of transport (COT), versatility, and energy consumption. For measuring power, the battery voltage, $V_{battery}$, and the battery current, $I_{battery}$, were measured.

$$P_{battery} = V_{battery} \times I_{battery} \tag{3.5}$$

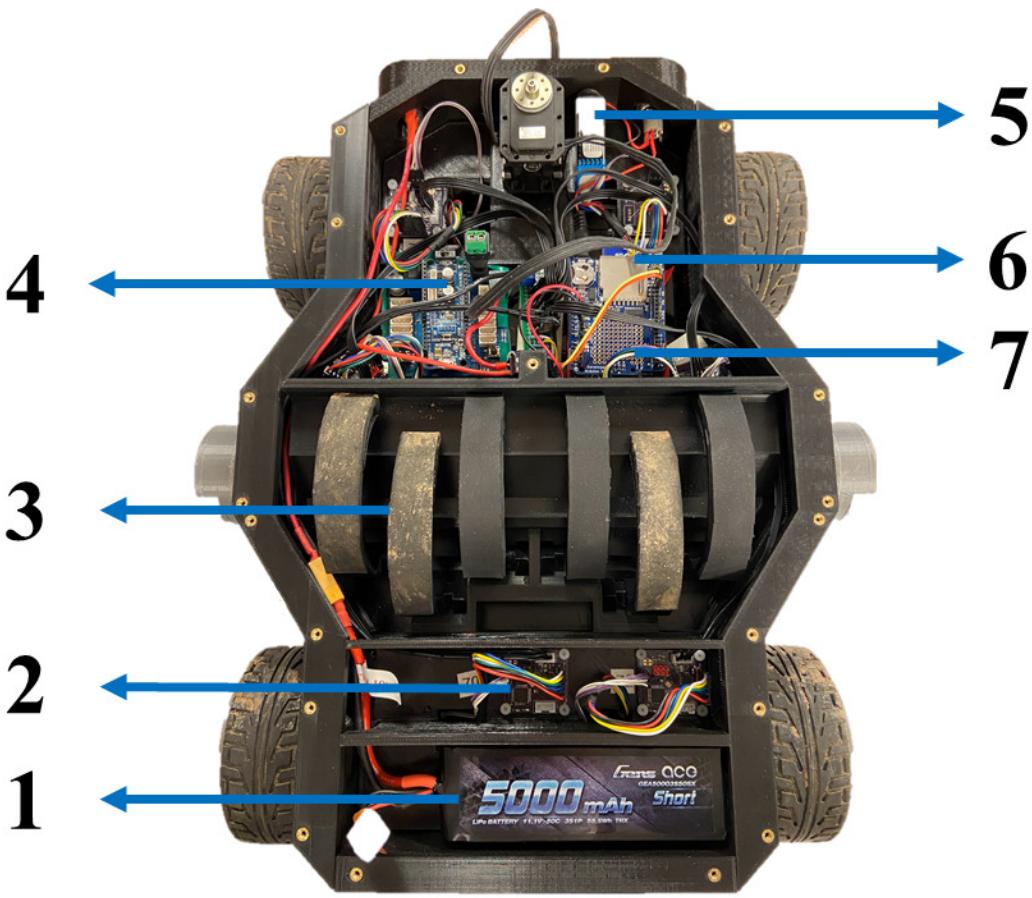

Figure 3.6: Annotated view of the internal components of the swappable propulsor prototype. 1) 11.1V Lithium Ion Battery; 2) custom-built I2C motor controller board; 3) storing base for propulsors; 4) OpenCM 9.04 Expansion Board; 5) 9V battery; 6) Adafruit Data Logger Shield; 7) Arduino MEGA 2560.

Cost of transport is the standard metric for comparing the energy consumption of mobile systems [44]. COT represents the power needed to travel at a certain speed. In this work, the input energy is electrical energy. The value is normalized using the mass, m, and the gravitational acceleration, g. A lower COT means more efficient use of energy.

$$\text{COT} = \frac{P_{battery}}{mg\,|v|} \tag{3.6}$$

As a prerequisite, the experiments required the identification of accessible terrain with large variations in friction, height, and grade. These were narrowed down to concrete,

grass, gravel, and forest that were readily available on the Georgia Tech campus. During the experiments, the robot operated on each terrain at maximum actuator speed over a fixed amount of time. Terrain, presence of manipulator, and mode of locomotion were varied in different combinations for each experiment. Each experiment had three trials and was averaged. The experiments are illustrated in the accompanying video [45].

3.5.2 Initial Comparisons

To initially compare the two modes of locomotion, this work examined the performance of wheels and legs on concrete. Experiments were performed by having the robot travel for $30s$ at maximum actuator speed ($200RPM$) on concrete while measuring distance/speed and power. The presence of the manipulator was varied as well. The results show that wheels have a relatively low COT (0.52) and can overcome small barriers. However, they cannot overcome larger obstacles that exceed the wheel diameter, such as a $127mm$ tall curb. The power consumption and COT for the wheeled mode do not change substantially when the manipulator is added. The results are summarized in Table 3.1 and shown in Figure 3.7. The legged performance had a substantially higher COT (3.4), mainly due to the slower speed. However, the legged mode enabled traversal over the curb which caused failure.

Table 3.1: Power Consumption Comparison for Adding Manipulator

Mode	**Power (W)**	**Mass (kg)**	**Velocity (m/s)**	**COT**
WHL[a]	21.52	4.8	0.883	0.517
WHL-A[b]	21.88	5.8	0.883	0.435
LEG[c]	29.32	4.8	0.184	3.389
LEG-A[d]	36.95	5.8	0.140	4.639

[a] WHL: Wheeled Locomotion.
[b] WHL-A: Wheeled Locomotion Manipulator Attached.
[c] LEG: Legged Locomotion.
[d] LEG-A: Legged Locomotion Manipulator Attached.

These basic results on concrete illustrate the overall advantages of the proposed method.

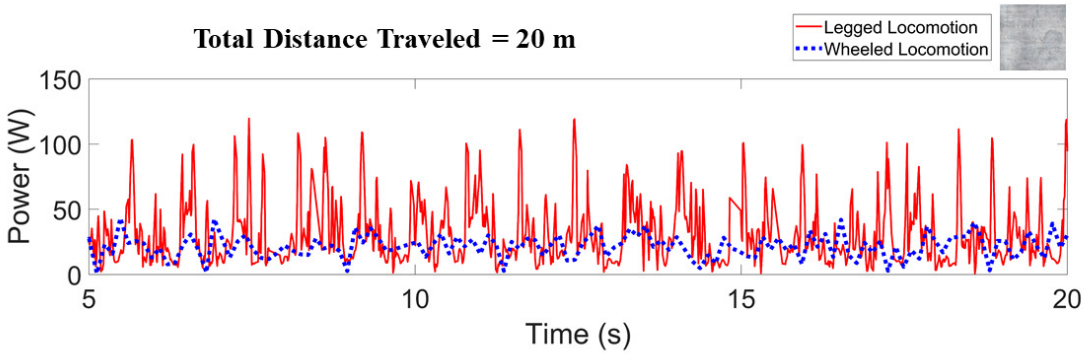

Figure 3.7: Power consumption measurements on flat concrete surface over 20 meters. The average power consumption for legged locomotion was 29.32 W. Average power consumption for wheeled locomotion was 21.52 W.

The legged mode is more robust to terrain but suffers from low energy efficiency. One approach would be to simply use the legs all the time. However, the energy benefits from using wheels are substantial, especially if long distances are anticipated. In addition, the presence of the manipulator on the vehicle does not substantially degrade the performance of the wheels. Therefore, the ability to use the manipulator more than pays for itself in terms of enabling energy efficiency.

3.5.3 Performance of Fully-Integrated System

Since the initial results validated the need for manipulation, further experiments were performed with the arm attached to the robot. This work conducted similar experiments on additional terrain including grass, gravel, and forest. These experiments exhibited similar trends to concrete. Unlike the previous work [42], the wheeled robot did not immediately fail on more complex terrain. This is due to the improved design; specifically, increased ground clearance and more powerful motors. However, the wheeled robot did fail in the presence of obstacles or on particularly challenging ground. The vehicle was unable to move forward in the presence of multiple logs and tall grass in forest terrain. The wheel mode had a slight degradation in COT on the other terrain. The wheels had a COT of 0.7

on grass, 0.8 on gravel, and 0.76 on forest (before being obstructed by obstacles). The results on traversable terrain are shown in Figure 3.8. The failure modes for the wheels are illustrated in Figure 3.9.

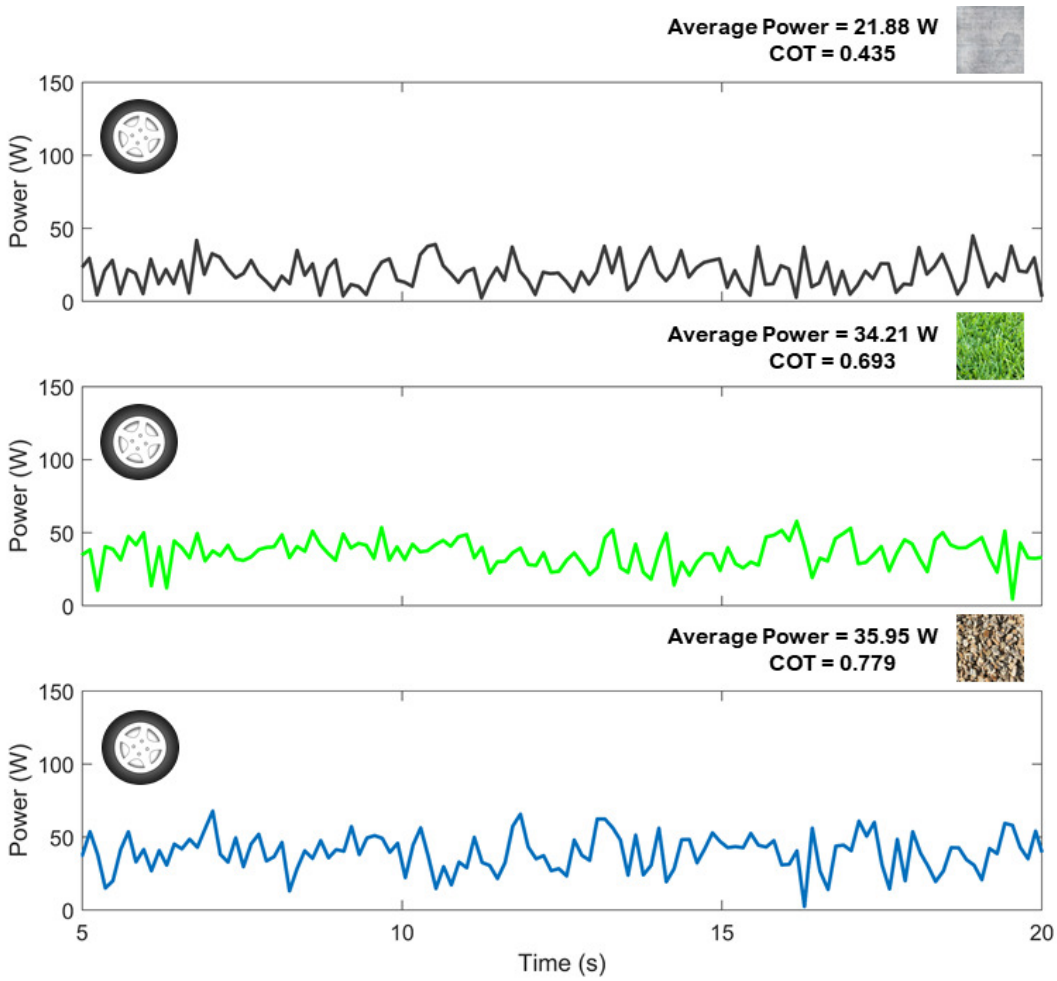

Figure 3.8: Power consumption of the wheeled mode on different terrain, operating at maximum speed.

Table 3.2: COT Comparison Table in Different Terrain

Mode	**Concrete**	**Grass**	**Gravel**	**Forest**
WHL[a]	0.435	0.693	0.779	∞
LEG[b]	4.639	5.015	5.363	5.793

[a] WHL: Wheeled Locomotion.
[b] LEG: Legged Locomotion.

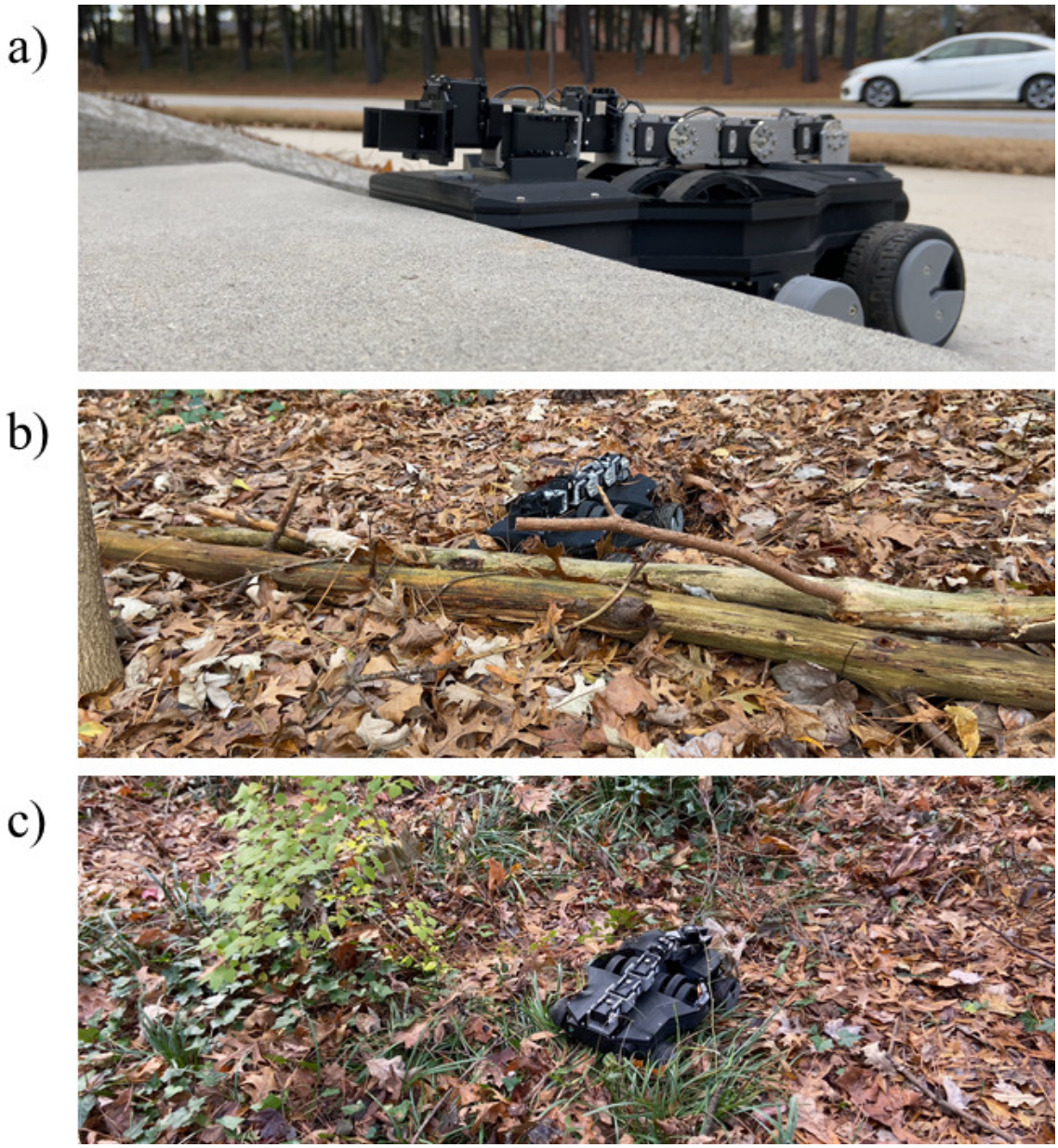

Figure 3.9: a) Wheels failing due to curb. b) Wheels failing to traverse forest terrain due to logs. c) Wheels getting stuck in tall grass.

The legged mode was examined on the same terrain, with a particular focus on the environments that caused the wheeled mode to fail (curb, logs, tall grass/forest). Specifically, additional experiments were performed on obstacles to highlight the capability of the robot and were performed until success was achieved. These results come in two forms: steady-state over relatively uniform ground, and specific results over a particular barrier.

The steady-state results are summarized in Table 3.2. Note how the COT is substantially higher than the wheels. Simply put, the results show that wheels either provide excellent energy efficiency or suffer from complete failure (no motion). Legs, on the other hand, have reduced efficiency but can handle more diverse environments. Data from the leg mode traversing each obstacle is shown in Figure 3.10. Photographic illustrations are also provided in Figure 3.11. The obstacle traversal data represents a clear extension of the team's past work in this area. The previous work did not examine obstacles in detail and did not attempt obstacles as large as the ones observed in this study (the curb exceeds the diameter of the wheel). While it is well known that a regular rHex robot can traverse such obstacles, the presented system has some clear differences. First, the legs are attached only with magnets, but the experiments showed that the attachment mechanism could handle the loads from moving over obstacles. Second, the presented system cannot flip over like many other rHex designs. This makes going over some obstacles more difficult. Lastly, the presence of the arm means that the mass distribution is non-uniform. Nonetheless, the robot was able to traverse obstacles that caused wheel failure.

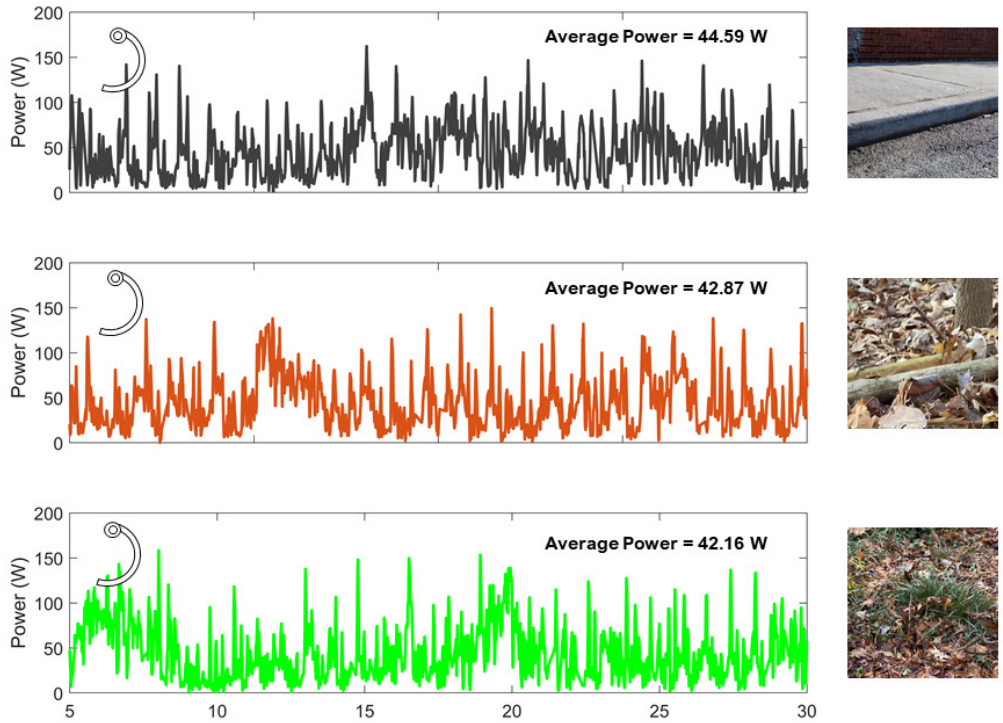

Figure 3.10: Electrical power data from the legged mode overcoming obstacles.

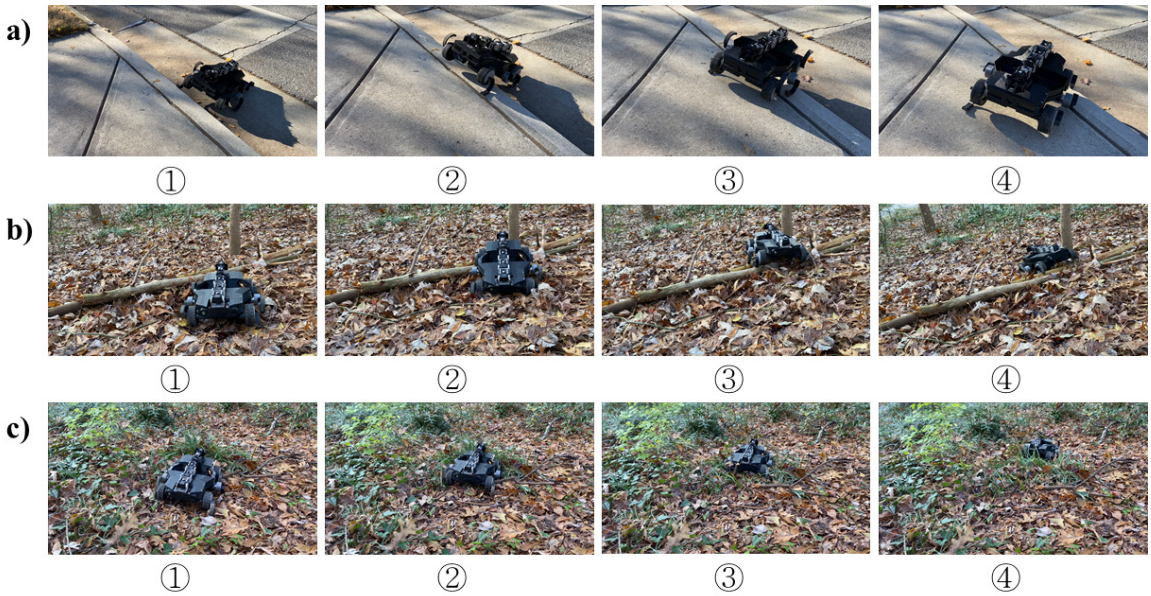

Figure 3.11: a) Legs overcoming the curb. b) Legs overcoming logs. c) Legs overcoming tall grass.

3.5.4 Manipulation for Physical Adaptation

The last step is to validate and quantify the actual physical adaptation. In this work, manipulation was achieved by replaying the hand-developed trajectories for each of the six propulsor mounts. The manipulator joint trajectories and the propulsor mount angles are stored onboard the robot microcontroller.

Closed-loop position control of the propulsor mounts is used to make sure they are aligned correctly. Similarly, closed-loop control was performed on the angles of each of the joints of the manipulator. The closed-loop control was performed by the servo-motors. This methodology is vulnerable to errors such as poor grasping of the propulsor, or dropping of the propulsor. These issues were not significant in this study, but need to be resolved for actual field implementation.

For attaching the legs, the motion consists of the following steps:

1. Move to the desired storage location of the swappable propulsor.
2. Close gripper to grasp swappable propulsor.
3. Remove swappable propulsor by exploiting geometric features (tilting) and pulling.
4. Move to wheel mount and attach using magnetic forces.
5. Slide the propulsor to constrain in wheel mount.

Note that for a reliable swapping process, each wheel rotates to its known desired position for optimal mounting and maintains its position. This process is repeated for each propulsor, with minor modifications for the attachment location. The steps for detaching the legs are similar and are outlined below:

1. Move to desired wheel mount location.
2. Close gripper to grasp swappable propulsor.

3. Slide the propulsor to release from the wheel mount.

4. Tilt the propulsor and pull the propulsor away from the wheel mount with minimal force.

5. Store propulsor in chassis.

The attachment trajectories are illustrated in Figure 3.12. These trajectories were designed in Cartesian space using human inputs and the corresponding joint angles were stored and used as commands to the manipulator joints. The figure shows the forward displacement analysis predictions based on these joint angles.

The entire attachment process for all six propulsors takes $80s$. The entire detachment process for all six propulsors also takes $80s$. Energy consumption during the swapping process was also evaluated by measuring battery voltage and battery current usage. Three trials were conducted for each process and the data sets were averaged. The power consumption during attachment and detachment is shown in Figure 3.13. The power consumption during attachment remains relatively flat. However, the spikes from detachment forces/torques are shown clearly. The total attachment energy is $820J$, and the total detachment energy is $840J$. For reference, the robot in wheeled mode could travel approximately $30m$ with similar energy consumption. Switching from legs to wheel and then back to legs consumes $\sim 1660J$ or the equivalent of traveling $60m$. Therefore if the obstacle-free path is substantially more than $60m$ than the one with obstacles, it may save energy to switch to the legged mode. The demonstration of the attachment and detachment process for all six propulsors are illustrated in the accompanying video [45] and in Figure 3.14 and Figure 3.15. The swappable propulsor was re-colored in post-processing to make it more visible in the figures.

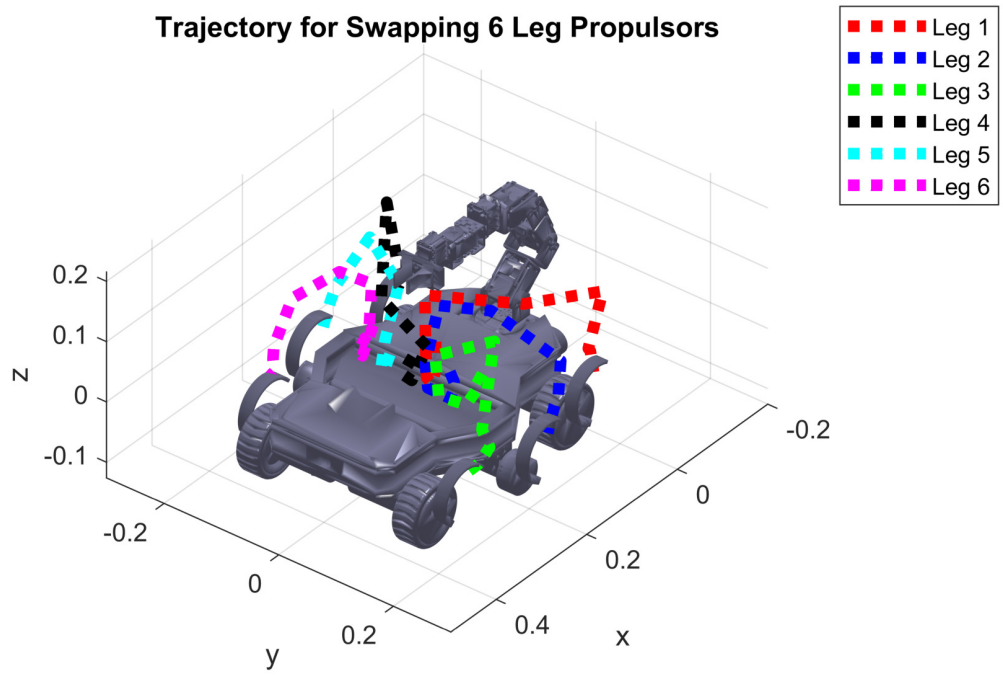

Figure 3.12: Illustrations of the manipulator's attachment trajectories relative to the vehicle body.

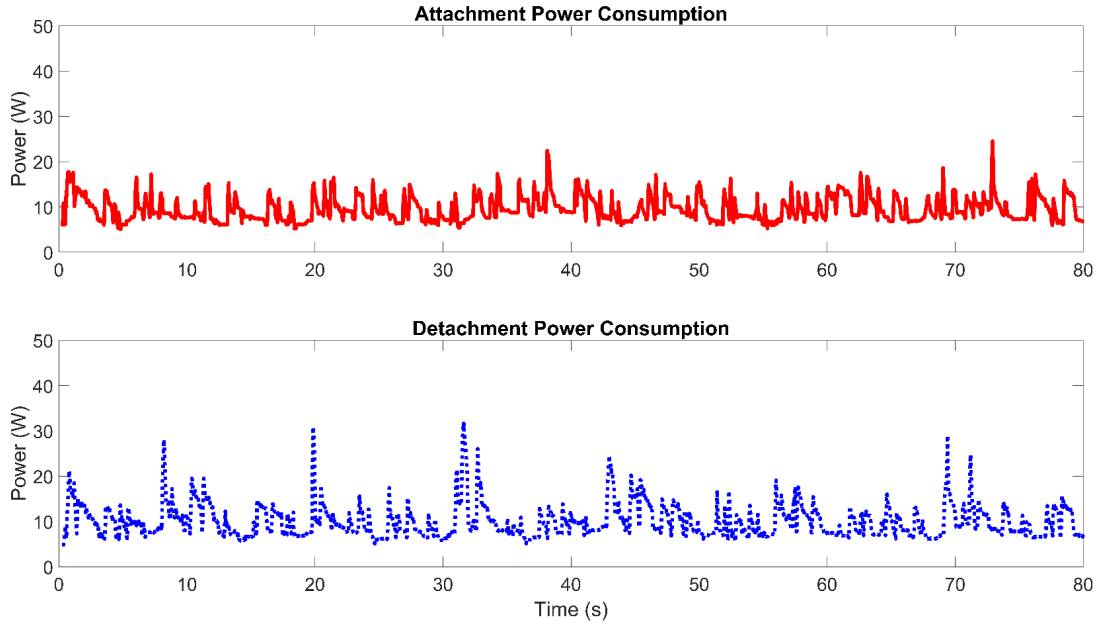

Figure 3.13: Power consumption during attachment (red) and detachment (blue).

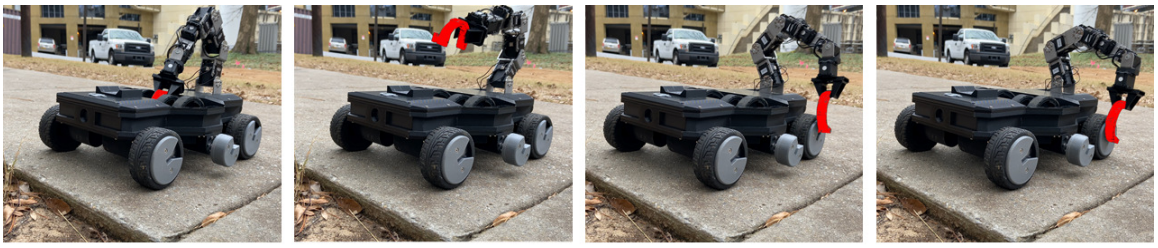

① ② ③ ④

Figure 3.14: A photographic illustration of the swappable leg-wheel propulsor robot attaching a leg propulsor is shown. 1) Grasp the leg propulsor inside the chassis. 2) Detach propulsor from storing base. 3) Attach the leg propulsor to the wheel. 4) Slide leg propulsor to constrain.

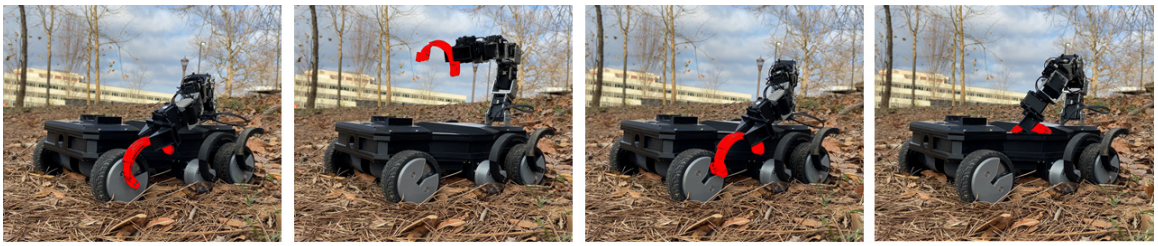

① ② ③ ④

Figure 3.15: A photographic illustration of the swappable leg-wheel propulsor robot detaching a leg propulsor. 1) Grasp desired leg propulsor. 2) Slide leg propulsor. 3) Detach the leg propulsor from the wheel. 4) Store leg propulsor inside the chassis.

3.6 Wheel-Wheg Hybrid Locomotion

The prototype previously shown demonstrated the transition between 4-wheeled locomotion and 6-legged locomotion, which requires the swapping of 6 propulsors. However, this process can be time-consuming and energy-intensive, particularly if an obstacle is minor along the path. To make the approach more feasible, the number of propulsors requiring replacement can be minimized by ensuring that the swappable propulsors complement the currently installed propulsor on the robot. This strategy reduces the energy consumed during manipulation. By choosing a reliable base propulsor, such as wheels or tracks, and attaching/detaching only a pair of propulsors to surmount a specific obstacle on a particular terrain, the overall energy efficiency and versatility of the system can both be significantly increased. An example of this approach is shown in Figure 3.16.

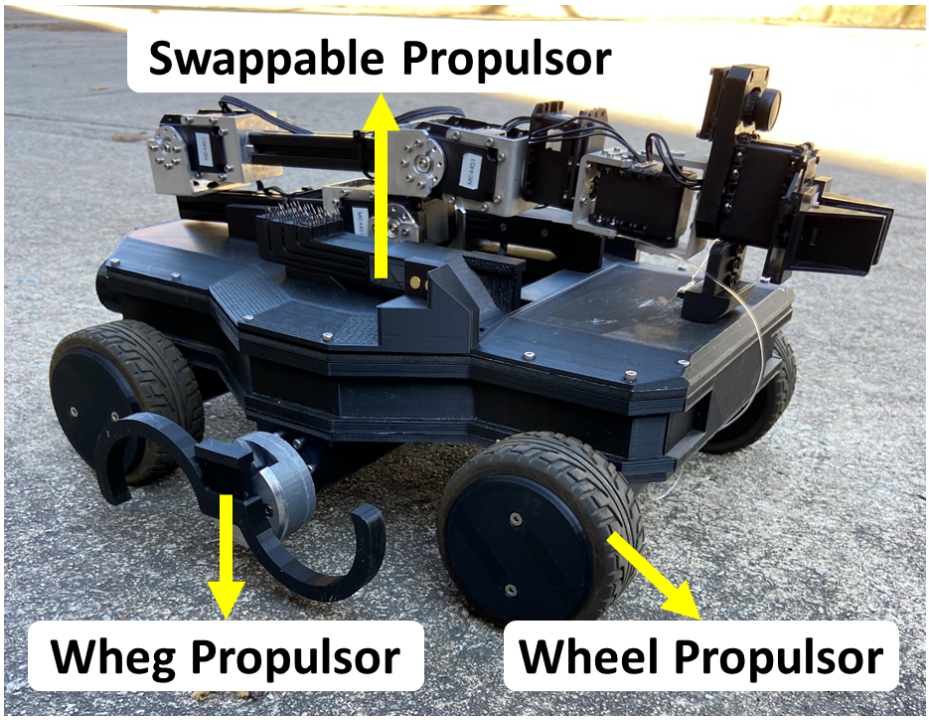

Figure 3.16: Physical prototype was reconfigured to enable more adaptations. Wheel propulsor was chosen as the base propulsor with wheg propulsors as the complementary propulsors. The storage space on the chassis enables another pair of swappable propulsors to be carried around for a unique obstacle that cannot be traversed by the wheg propulsors.

The prototype was reconfigured for wheel-wheg hybrid locomotive capabilities in this study. Wheel propulsors were selected as base propulsors, and a pair of swappable wheg propulsors were installed on the middle pair of actuators which were initially used to enable 6-legged locomotion. This approach provides several advantages. Wheel propulsors provide energy-efficient locomotion across flat terrain while swappable wheg propulsors can be actuated to overcome obstacles with a height greater than the wheel's diameter. These wheg propulsors can remain on the steel surface mounts and only need to be swapped with a different swappable propulsor from its chassis when it encounters a unique obstacle that the wheel-wheg hybrid locomotion cannot overcome. Overall, the average COT for this configuration is equivalent to the 4-wheeled locomotion, and the energy needed to swap propulsors reduces by a third of what it took to swap out 6 propulsors. The energy consumed to swap out a pair of propulsors is shown in Figure 3.17. The total energy consumed

during the process is approximately $1060J$.

Figure 3.17: Power consumption during swapping of two pairs of swappable propulsors.

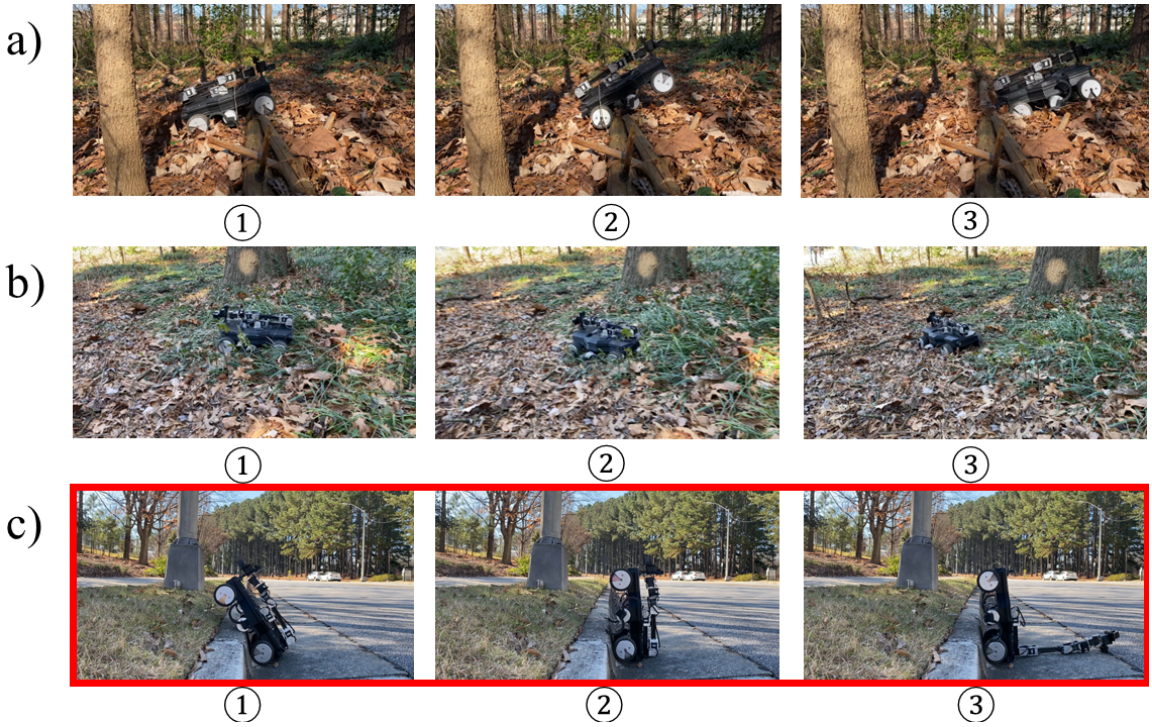

Figure 3.18: (a) Wheel-whegs overcome logs. (b) Wheel-whegs enable traversal through tall grass/forest. (c) The robot fails to overcome the curb due to the mass of the manipulator.

The newly configured prototype was examined on the same terrain, with the same particular focus on the environments that caused the wheeled mode to fail (curb, logs, tall grass/forest). The overall COT of the configuration had the same COT as the 4-wheeled locomotion. The wheel-wheg hybrid locomotion was able to overcome the logs and the tall

grass/forest terrain, much like the 6-legged locomotion. However, this configuration was not able to overcome the curb. A photographic illustration is shown in Figure 3.18.

3.6.1 Climbing the Curb

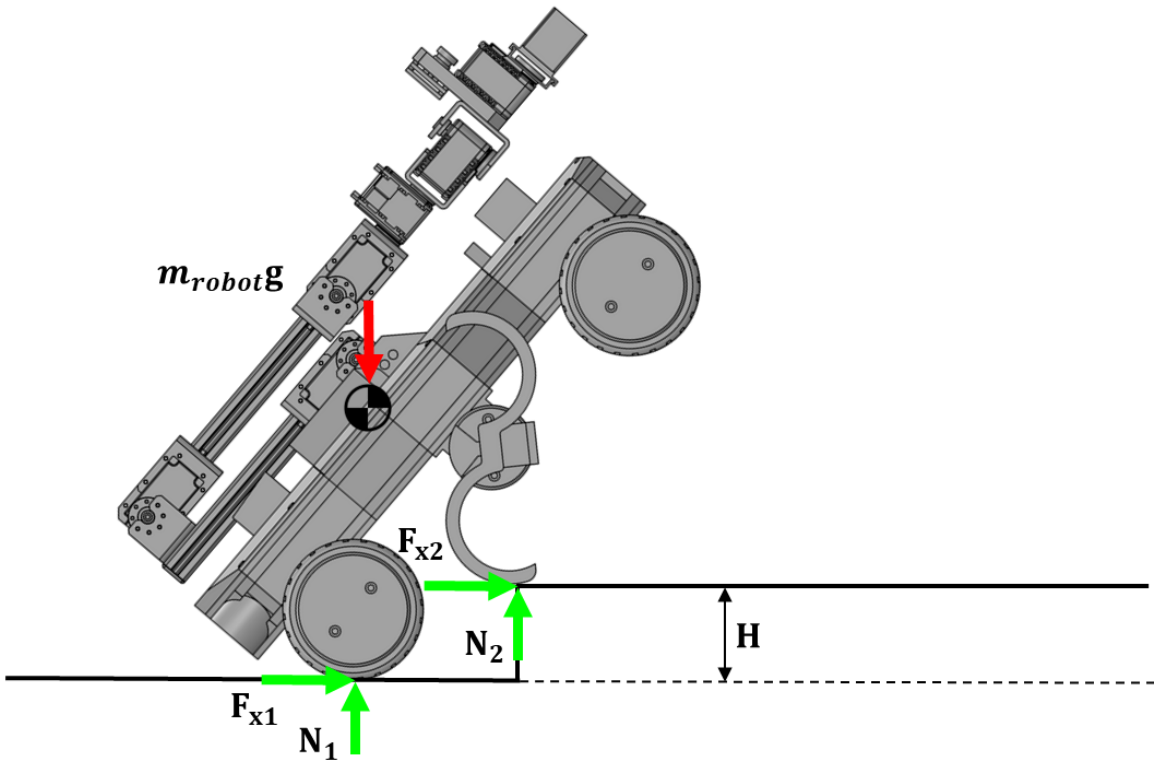

Figure 3.19: Diagram of the robot climbing a curb.

The experiments demonstrated that the wheel-wheg prototype failed to overcome the curb. At critical height, the mass of the manipulator creates a backward moment which causes the robot to flip backward. This is illustrated in Figure 3.19. However, by reconfiguring the manipulator and shifting the center of mass of the arm, the robot can mitigate this failure, increasing the versatility of the system.

The following steps are necessary for the wheel-wheg mobile robot to traverse a curb:

1. The front end of the robot climbs onto the curb.

2. The rear end of the robot climbs onto the curb with the propulsion of the whegs.

3. The robot lands on the ground without flipping.

Figure 3.20 shows a force diagram for the condition when the robot is stationary at the time the front wheel starts to move up along the curb. N_A and N_B are normal forces applied to the robot from the ground and the curb; F_A and F_B are the static friction experienced by the wheels from the ground and the curb; and m_{robot}, R, d, and l are the mass of the robot, the radius of the wheel, and the distance between the curb and the center of mass (COM) and the rear wheel to the curb, respectively.

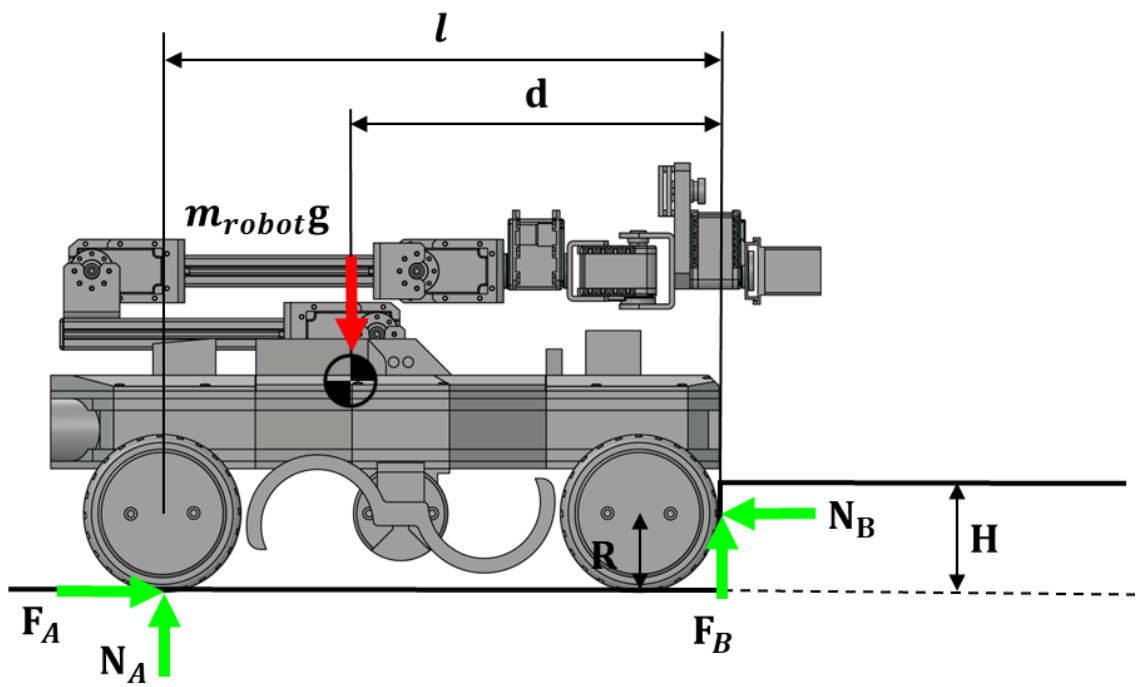

Figure 3.20: Force diagram when the robot stops at the time the front wheel starts to move up along the curb.

Since the horizontal and vertical forces are balanced inFigure 3.20, $F_A = N_B$ and $N_A + F_B = m_{robot}g$ (where g is the acceleration of gravity). Considering moment equilibrium about the point of contact on the curb, $N_A l - m_{robot}gd - F_A R = 0$ holds. Rearranging and substituting, the following can be found.

$$N_A = \frac{m_{robot}gd + F_A R}{l} \tag{3.7}$$

$$F_B = mg - \frac{m_{robot}gd + F_A R}{l} \tag{3.8}$$

The conditions for the robot to not slip on the ground and curb are $F_A < \mu_A N_A$ and $F_B < \mu_B N_B$, respectively, where μ_A and μ_B are the coefficients of static friction of the ground and the curb. Therefore, the larger value of d in Equation 3.7 and Equation 3.8 allows the conditions to be easily met. This means the backward-positioned COM can prevent the wheels from slipping on the ground and the curb, thus providing large propulsion needed to achieve Step 1. Since μ_A and μ_B depend on the surfaces of the terrain and the curb, respectively, the conditions $F_A < \mu_A N_A$ and $F_B < \mu_B N_B$ are variable according to the environment. For the specific prototype used in this study, if the coefficient of friction is insufficient to lift the robot, the wheg propulsor can be actuated to elevate the vehicle.

3.6.2 Shifting the Center of Mass for Obstacle Traversal

To analyze step 2 and enable climbing of the curb, the geometric boundary conditions can be analyzed to find the optimal COM location. Figure 3.21 illustrates the instance in which the robot is climbing the curb with height H, at a constant velocity, with the vehicle-mounted manipulator extended forward. F_{x1} and F_{x2} are the friction forces applied to the ground and the curb by the wheels and the whegs respectively. N_1 and N_2 represent the normal forces applied to the robot. $m_{vehicle}$ and m_{arm} are the mass of the vehicle and the manipulator. L, R and r are the length of the vehicle, and radii of the wheels and the whegs respectively. θ and ϕ represent the angle of elevation of the vehicle and the angle of rotation of the wheg respectively. a and b are the normal distances from the center of the wheg to the COM of the vehicle and the arm respectively. x and z represent the COM location of the arm which can be used to calculate the joint configurations of the manipulator.

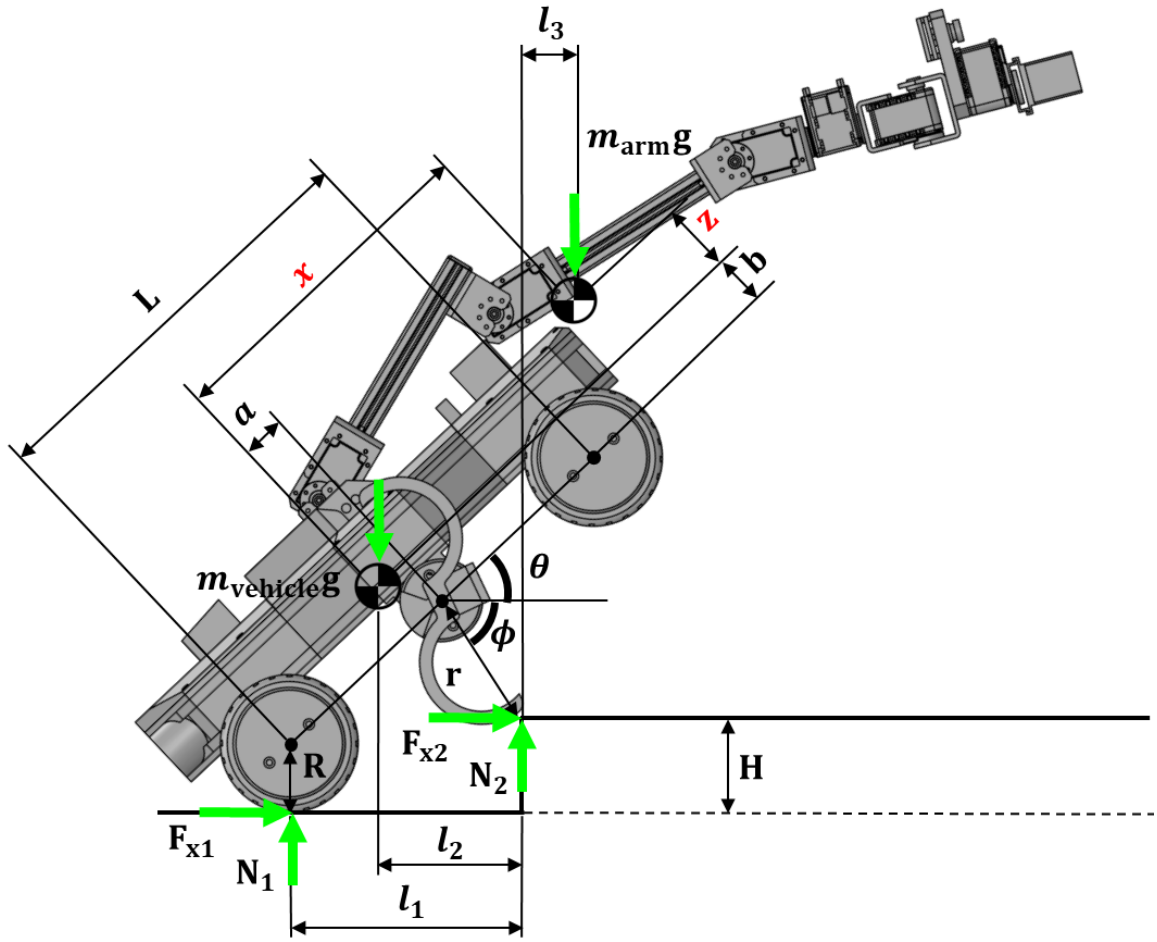

Figure 3.21: Diagram of the robot with an extended manipulator configuration climbing a curb. The robot can shift the center of mass by changing the arm configuration.

By analyzing the moment about the point in which the wheg makes contact with the curb, the boundary condition that produces the maximum clockwise moment for climbing can be found. The geometric parameters to obtain this boundary condition is represented in Equation 3.9, Equation 3.10, and Equation 3.11.

$$l_1 = \frac{L}{2}cos\theta + rcos\theta \tag{3.9}$$

$$l_2 = acos\theta + bsin\theta + rcos\phi \tag{3.10}$$

$$l_3 = xcos\theta - l_2 - zsin\theta \tag{3.11}$$

Equation 3.12 and Equation 3.13 represent the horizontal forces and vertical forces balanced in Figure 3.21, with $F_{x1} = \mu_{wheel} N_1$ and $F_{x2} = \mu_{wheg}$. μ_{wheel} and μ_{wheg} represent the coefficient of friction of the wheels and whegs against the ground and curb respectively. If the coefficient of friction values decrease, say due to weather/terrain, the maximum height value that the robot can overcome decreases. The moment about the point at which the wheg makes contact with the curb is defined in Equation 3.14 with the previously defined geometric parameters l_1, l_2, and l_3.

$$\sum F_x = F_{x1} + F_{x2} = 0 \tag{3.12}$$

$$\sum F_y = N_1 + N_2 - m_{vehicle} g - m_{arm} g = 0 \tag{3.13}$$

$$\sum M_{contact} = F_{x1} H + m_{vehicle} g l_2 - N_1 l_1 - m_{arm} g l_3 = 0 \tag{3.14}$$

By rearranging Equation 3.14, the COM of the arm x and z which produces the maximum clockwise moment to climb the curb can be found. This is represented in Equation 3.15.

$$F_{x1} H + m_{vehicle} g l_2 < N_1 l_1 + m_{arm} g l_3 \tag{3.15}$$

Using these boundary conditions, a range of possible COM locations were found for the wheel-wheg propulsor prototype. To obtain values that were feasible, the simulation included self-collision constraints and conditions that bounded the manipulator from touching the ground. These values are shown in Figure 3.22 and Figure 3.23. The COM locations x and z that produce the maximum clockwise moment were calculated to be $0.2763m$ and

$0.0495m$ respectively.

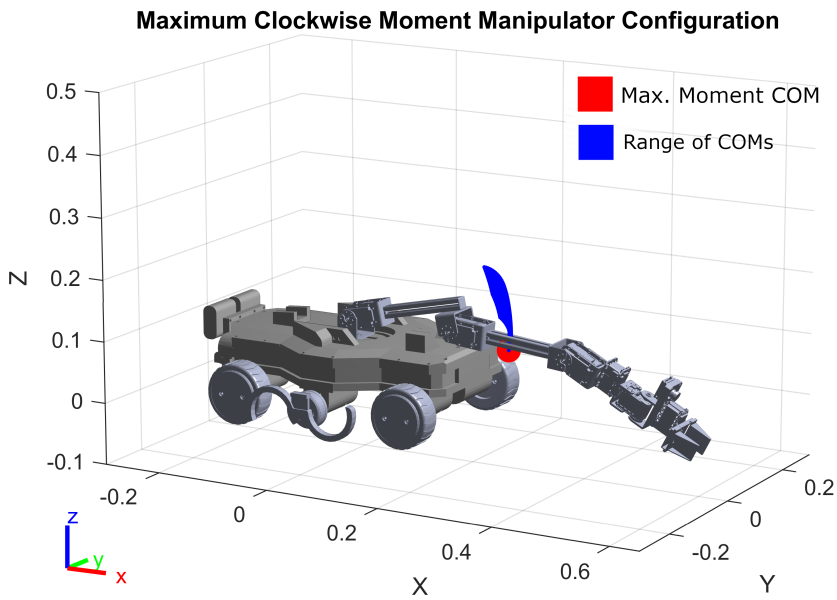

Figure 3.22: Plot showing the arm configuration that produces the maximum clockwise moment.

3.6.3 Simulation and Experiments

Simulations and physical experiments were carried out to evaluate and validate the analysis. The simulation was run on ROS Noetic Gazebo with model parameters experimentally obtained from the physical prototype. The simulation parameters used are outlined in Table 3.3. The physical interactions of the model with different manipulator configurations were replicated in the simulation. These are illustrated in Subfigure 3.24(a), Subfigure 3.24(d), and Subfigure 3.24(e). After validating the analysis in simulation, the maximum COM location was tested on the physical prototype. The results are shown in Figure 3.24.

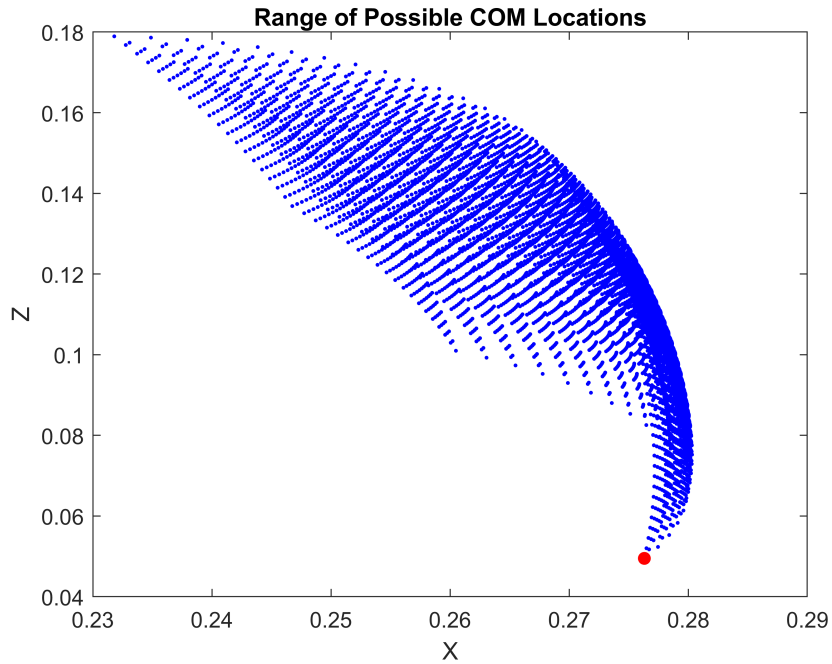

Figure 3.23: Plot illustrating the ranges of the possible COM locations with the self-collision constraints and ground constraints.

Table 3.3: Model Parameters in Gazebo

Parameter	**Value**
L	0.303 (m)
a	0.0115 (m)
b	0.0413 (m)
R	0.05 (m)
r	0.08 (m)
H	0.15 (m)
x	0.2763 (m)
z	0.0495 (m)
$m_{vehicle}$	5.6 (kg)
m_{arm}	1.086 (kg)
μ_{wheel}	0.7
μ_{wheg}	0.6

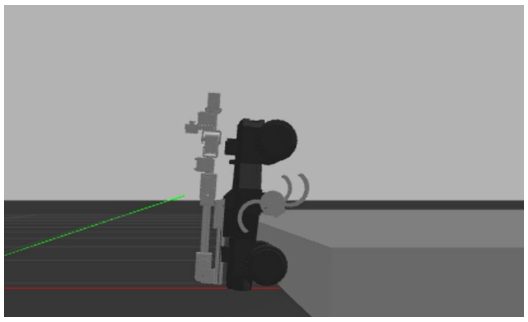

(a) Robot is unable to climb in simulation.

(b) Robot is unable to climb the curb.

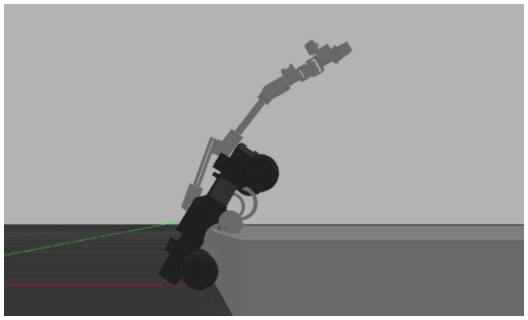

(c) Manipulator is extended in simulation.

(d) Manipulator is extended to COM location.

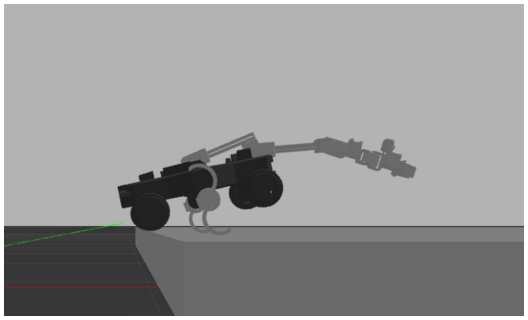

(e) Robot successfully climbs in simulation.

(f) Robot successfully climbs the curb.

Figure 3.24: Simulation and experiment of climbing the curb using the COM locations found. The height used in this simulation is $0.15m$. (a) & (b) Robot is unable to climb the curb in default manipulator configuration. (c) & (d) Manipulator is extended to a possible COM location. (e) & (f) Robot successfully climbs the curb with extended configuration.

3.7 Diversifying Swappable Propulsors

This section presents the different types of swappable propulsors that can be used across different surfaces. Specifically, this section presents swappable propulsor designs that enable traversal over obstacles that wheels and whegs cannot overcome. Figure 3.25 illustrates two distinct propulsor designs, which draw inspiration from existing solutions. The propul-

sors are paired and designed to complement the wheel propulsors, reducing the number of swaps while maintaining efficacy.

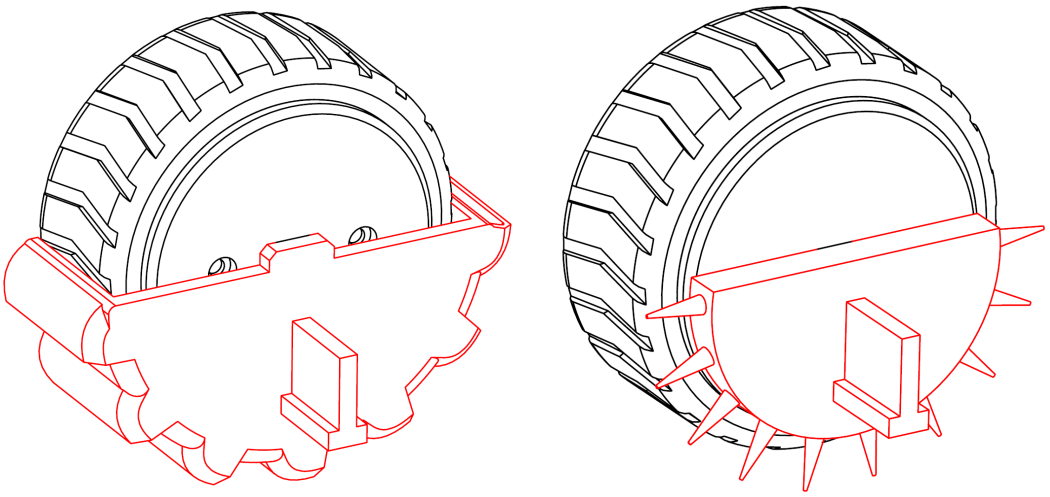

(a) (b)

Figure 3.25: (a) Swappable Sand Propulsor. (b) Swappable Spike Propulsor.

3.7.1 Swappable Sand Propulsor

Mobile robots operating on soft soils such as sand face significant challenges due to the dynamic effects occurring at the wheel-terrain interface. When traversing soft, granular media, a mobile robot may experience substantial slip and sinkage causing performance failure [46, 47]. These failures are caused by the reduction in traction from the ripples and fine-grained sediments inside the feature. This is shown in Subfigure 3.26(a). Numerous existing solutions are available to address the aforementioned issue, including but not limited to reducing tire pressure to augment traction [48], implementing sand paddles or spokes [49], or navigating with tracks. To facilitate the physical adaptation of the existing wheels, a swappable sand propulsor with paddles was designed. Experiments were conducted on sand terrain available on Georgia Tech campus to validate the usage. An illustration of the experiments is shown in Subfigure 3.27(a). To traverse on sand, the wheel-wheg configuration needed to consistently use the 4 wheels and the pair of whegs in

order to move forward. The average COT resulted in 1.369. By attaching a swappable sand propulsor on a pair of wheels, the robot was able to traverse sand with an average COT of 0.887. Using the complementary sand propulsor resulted in a lower COT due to fewer actuators being used and covering more distance in the same given amount of time. The use of whegs caused a reduction in speed due to longer spokes causing the robot to elevate vertically.

3.7.2 Swappable Spike Propulsor

Mobile robots operating on slippery surfaces such as ice face significant challenges due to the reduced traction between the wheels and the ground. Wheel slip is inevitable when a mobile robot is moving at a high speed or on a slippery surface. Specifically, these surfaces with low coefficients of friction can cause performance degradation with acceleration, stopping, or turning [15]. Subfigure 3.26(b) illustrates how the wheels and wheg propulsors have no efficacy in increasing traction to mitigate slip. A recent publication presented an active-adaptive solution that deployed spikes to increase traction, enabling the vehicle to accelerate 171% faster than tires. To facilitate the physical adaptation of the existing wheels, a swappable spike propulsor was retrofitted. Experiments were conducted on polysynthetic ice to validate the usage. An illustration of the experiments is shown in Subfigure 3.27(b).

(a) (b)

Figure 3.26: (a) Wheels can slip or get stuck in soft, granular media such as sand. (b) Whegs/wheels slip on surfaces such as ice, which can significantly reduce performance.

(a)

(b)

Figure 3.27: (a) Swappable Sand Propulsor displaces granular media to propel the vehicle forward. (b) Swappable Spike Propulsor uses spike insertions to increase traction with the slippery surface.

CHAPTER 4

MANIPULATION FOR INCREASED PAYLOAD CAPACITY AND VERSATILITY

Figure 4.1: (1) Vehicle-mounted manipulator can localize and attach the payload to the vehicle. (2) An anchoring device can be engaged on a given surface to increase payload capacity. (3) The anchoring device can be swapped using the manipulator for a different surface. (4) The robot can pull the payload on a different surface using a different anchor.

4.1 Swappable Anchor Framework

4.1.1 Functional Requirements

This section outlines the general functional requirements needed for the swappable anchor framework. Swappable anchors are devices that engage with a given surface to increase the coefficient of friction. Specifically, the anchor must be able to handle resistive forces from the payload, must be detachable, and must not consume energy. Swappable anchors offer solutions for increasing vehicle traction on various surfaces, and a few examples are shown in Figure 4.2. This figure illustrates how anchors can be designed to increase friction on (a) rough surfaces with asperities, (b) wet, muddy surfaces, (c) flat, smooth surfaces, and (d) soft, granular surfaces. The presented framework assumes that a mobile robot can store and carry multiple sets of swappable anchors, each associated with a particular surface. We defined the following functional requirements for an efficacious swappable anchor design:

1. **Increase coefficient of friction between the system and the surface.** The anchors should enable a mobile robot to pull loads that are substantially greater than the robot's mass. Once engaged, the surface contact of the anchors should increase the overall vehicle traction.

2. **High-holding force and zero power consumption during engagement.** When engaged, the anchors must remain attached to the robot to maintain effective contact with the surface. Maintaining the engagement of the anchoring device should not require energy consumption.

3. **Low force detachment using manipulation.** To pull loads on various surfaces, anchors must be swappable using a vehicle-mounted manipulator. Manipulators have force/weight limitations, so the detachment force should be sufficiently less than the minimum holding force.

4. **Reversible Anchoring.** The mobile robot should be able to unanchor itself. This is

needed to maintain robot mobility and enable payload transportation across various surfaces.

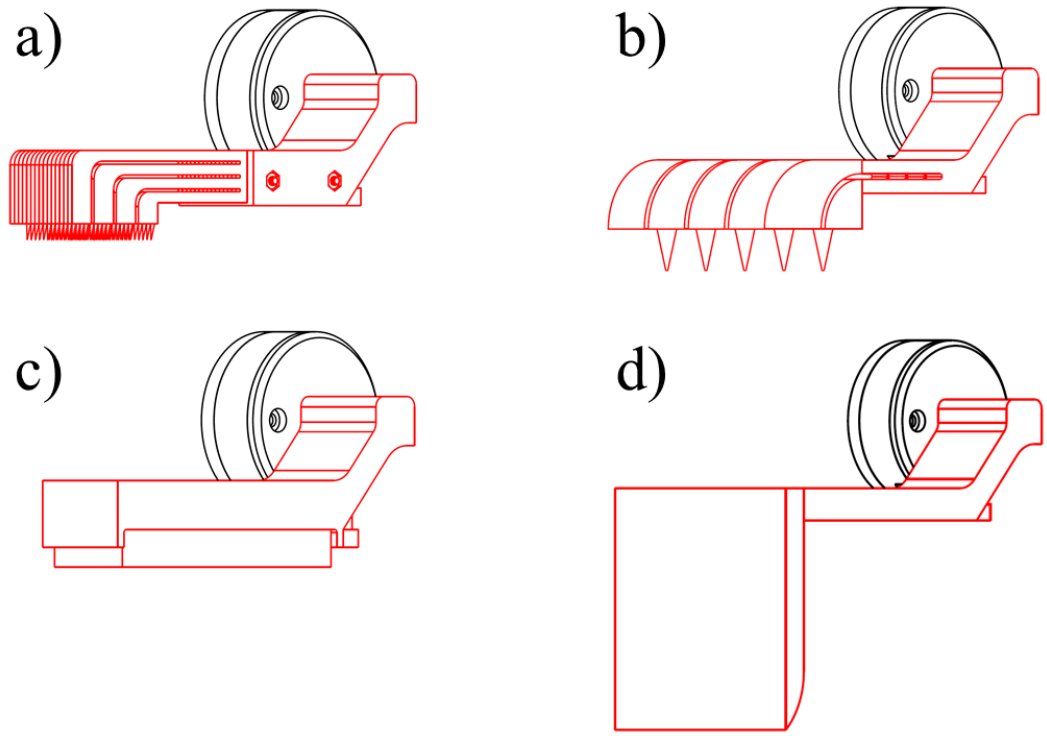

Figure 4.2: a) Microspine anchor; b) macrospine anchor; c) adhesive-rubber anchor; d) sand anchor. This figure illustrates how a range of swappable anchors can be designed for a particular surface. A range of swappable anchors (red) can be attached to a single housing (black).

4.1.2 Permanent Magnets with Mechanically Constraining Steel Surface Mounts

The mounting design described in the swappable propulsor framework [50, 51] satisfies the aforementioned functional requirements 2) and 3). As a result, this work adapts the swappable propulsor mounting design onto swappable anchors to enable reliable attachment and easy detachment with permanent magnets and geometric features.

To ensure reliable attachment, this mechanism leverages permanent magnets with ferrous steel surface mounts and T-slots. Permanent magnets with ferrous steel enable large attachment forces with low added mass and zero static power consumption. The design

limits undesired detachments in unwanted directions by using mating features with T-slots and mechanical frames. For easy detachment, the vehicle-mounted manipulator is used to overcome the magnetic attachment force. By exploiting geometric features, we can reduce the amount of force needed to overcome the attachment force. Specifically, we can use a large moment arm to decrease the magnetic attachment force by creating an air gap.

4.1.3 Anchor Design for Payload Transport

We can enable reversible anchoring by attaching anchors to the center actuators. The anchors can be rotated to engage the surface during payload pull and disengaged during motion. To maximize payload capacity, the swappable anchor must utilize an optimized surface contact with a high coefficient of friction, resist vehicle displacement, and maintain reliable contact with the surface. We can ensure the anchors maintain contact with the surface without any energy consumption by shaping the anchor such that the tensile force from the winch causes the anchors to dig deeper into the surface. Figure 4.3 illustrates the design of the anchor used in this study and the forces in play during a stable payload pull.

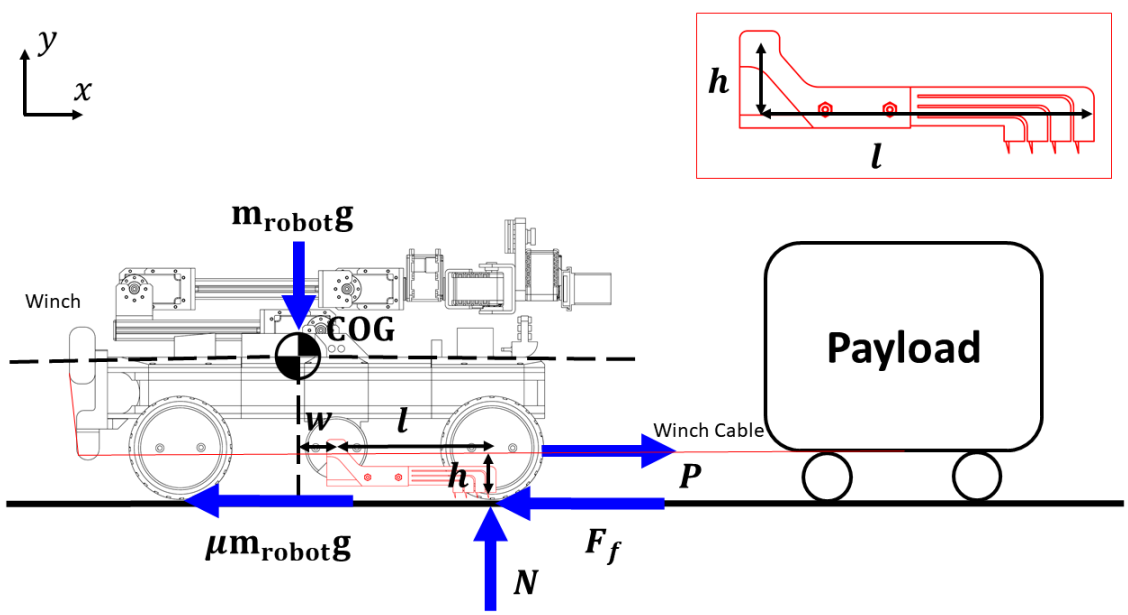

Figure 4.3: Force diagram representation of the vehicle pulling the payload using the winch.

$$\sum F_x = 0 = \mu m_{robot} g + F_f - P \tag{4.1}$$

$$\sum F_y = 0 = m_{robot} g - N \tag{4.2}$$

$$\sum M_{actuator} = 0 = m_{robot} g w + N l - (F_f + \mu m_{robot} g) h \tag{4.3}$$

$$\sum M_{anchor} = 0 = m_{robot} g (w + l) - P h \tag{4.4}$$

μ represents the coefficient of friction of the tires. m_{robot} and P represent the mass of the robot and the force of the payload respectively. We use h to represent the height of the anchor. l represents the length of the anchor and w is the horizontal distance from the center actuator to the center of mass. We denote F_f as the friction force and N as the normal force of the wheels and anchors.

The static force balance for the x and y directions are provided in Equation 4.1 and Equation 4.2. Equation 4.3 depicts moments about the center actuator during payload pull. When pulling substantially heavy loads, the friction forces may be large enough to generate a clockwise moment and results in the anchor digging into the surface.

While this design can improve anchoring, the moment around the tip of the anchor can cause the vehicle to flip over. Flipping over can degrade performance and may prevent the robot from recovering its mobility. Therefore, we need to determine geometric parameters that prevent flipping under expected loads.

Given a vehicle with known dimensions and a goal maximum payload, we can select the dimensions of the anchor, h, l, such that the moment caused by the payload does not flip the vehicle. Equation 4.4 denotes the condition that must be maintained to ensure the tensile force from the winch does not create a moment and lift the robot during the pull.

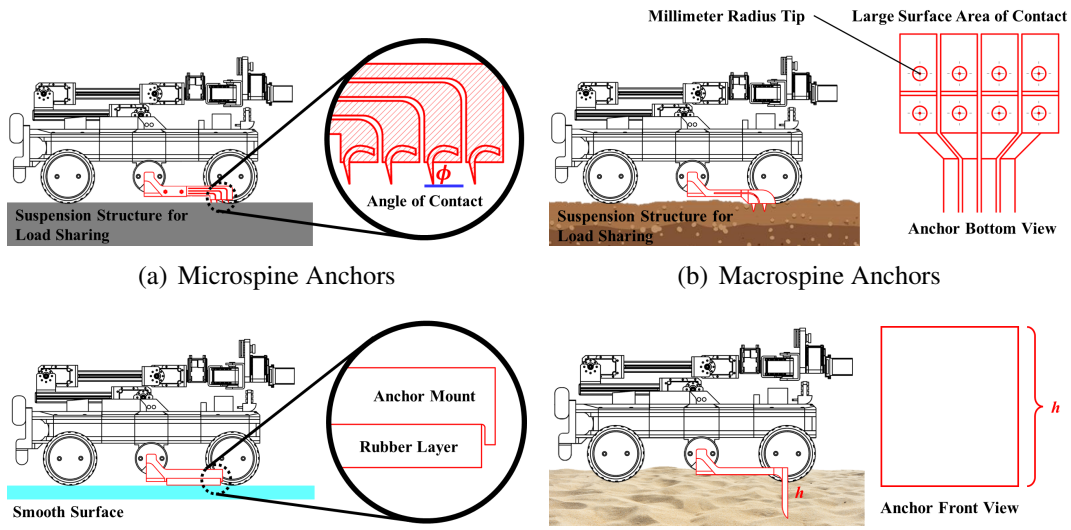

(a) Microspine Anchors (b) Macrospine Anchors

(c) Adhesive-Rubber Anchors (d) Sand Anchors

Figure 4.4: Anchor designs explored in this work. (a) Each layer has 4 microspines embedded. To handle the maximum shear load, the microspines are inserted such that the angle of contact, $\phi = 90 \sim 155\,\mathrm{deg}$. (b) Macrospine anchors use millimeter range radius tip spikes to pierce into wet, cohesive surfaces. Once submerged, large surface area of contact minimizes erosion of the surface. (c) Adhesive-rubber anchors consist of two layers, the anchor mount, and the rubber layer. (d) Sand anchors utilize greater insertion depth (h) to result in higher vehicle traction.

Substituting and rearranging Equation 4.4, we can obtain the set of possible dimensions for h and l that can be used to prevent flipping under expected loads. This is denoted in Equation 4.5.

$$\frac{m_{robot}g}{P} = \frac{h}{w+l} \tag{4.5}$$

4.2 Tailored Optimized Traction Mechanisms for Various Terrain

Varying terrain conditions are each associated with an optimal traction mechanism. We identify optimized traction mechanisms from the existing literature and customize them for swappable use on a mobile robot.

4.2.1 Hard Rough Surface Contact Design

For hard rough surfaces, the existing literature has already provided an excellent traction mechanism. Specifically, microspines are effective surface contacts for increasing friction on hard, rough surfaces such as concrete or rocky terrain [12]. Microspines consist of one or more hooks embedded in a rigid frame with a compliant suspension system. By arraying tens or hundreds of these microspines, large loads can be supported and shared between many attachment points. Since each spine has its own suspension structure, it can stretch and drag relative to its neighbors to find a suitable asperity to grip. While most previous microspine works have focused on low normal force (climbing applications) or low total force (microbots), our application focuses mainly on high coefficient of friction while supporting large normal loads. This will maximize ground friction and bear high tensile loads from the winch during payload pulling.

To create a microspine anchor that can efficiently and effectively increase the friction between the vehicle and the surface, we follow the design principles detailed in works [52, 38]. Since much of the design and analysis of the microspines have been researched already, we do not repeat them here. The design of the microspine anchor used in this work is shown in Subfigure 4.4(a).

4.2.2 Wet Cohesive Surface Contact Design

Wet, cohesive surfaces such as mud, forest soils, marshes, littorals, estuaries, and wet fields are ubiquitous in nature. These surfaces have properties changing in space and time, due to their infinite number of possible compositions. Therefore, deriving a general model for mud is complex and unpractical. Instead, we design a solution based on existing literature and empirically evaluate its efficacy and performance. In this work, we present a macrospine surface contact solution that enables increased stationary vehicle traction.

Macrospines consist of steel hooks with larger radius tips in the millimeter range. These millimeter range spikes, in comparison to microspines, can pierce deeply through the cohe-

sive terrain without completely destroying the cohesion of the surface. Once the spikes are submerged, the anchor makes large surface area of contact with mud, holding any erosion that may occur in place.

Results from [53, 54] show that the relationship between submersion and friction on mud can be approximated by a linear relationship whose slope is dependent on water content. Hence, we require a surface contact that can sink into the surface for high vehicle traction. These studies also illustrated how too stiff or too soft contact does not provide as much support force as intermediate stiffness. If the contact is too stiff, it either erodes the surface or slips. Too soft, it loses traction. Therefore, our proposed design uses a suspension structure much like the microspines to passively distribute the load across spikes and to prevent erosion of the surface. The design of the macrospine anchor used in this work is shown in Subfigure 4.4(b).

4.2.3 Smooth Surface Contact Design

Studies from [38] have demonstrated that high-friction, long-wearing rubber is effective in supporting large normal loads with a high coefficient of friction on flat smooth surfaces. This work utilizes abrasion-resistant polyurethane rubber as surface contact. The design of the adhesive rubber anchor is shown in Subfigure 4.4(c).

4.2.4 Granular Surface Contact Design

To increase vehicle traction on soft, granular media such as sand, we follow the principles outlined in [37] to design our surface contact. The study illustrates how an anchoring device can be utilized to increase insertion depth, h, which results in increased resistive force. Greater insertion depth leads to larger normal loads with a higher coefficient of friction. The design principles suggest two methods for maximizing insertion depth, static insertions, and dynamic impact. The static insertions method is well aligned for this study, due to the anchor design. The winch tension causes the anchors to dig deeper into the surface,

increasing insertion depth. The design of the sand anchor is shown in Subfigure 4.4(d).

4.3 Implementation

This section describes the implementation of this new approach to payload transport. The custom prototype vehicle described in this work is designed to increase the overall payload capacity of the system across various terrain using four different swappable anchors. In addition, we describe a high-level planner that is used to demonstrate payload transport through autonomous payload attachment.

4.3.1 Prototype Vehicle

This work utilizes a four-wheeled vehicle with two actuators extruding at the center of the chassis for reversible anchoring. The prototype vehicle can carry two pairs of anchors (one on the chassis storage space, and the other on the actuators). The prototype vehicle is shown in Figure 4.5. The wheels are driven by $50 : 1$ metal geared $12V$ DC motors. The center actuators are driven by $150 : 1$ metal geared $12V$ DC motors. The wheels are $105mm$ wide. Rubber tires are used on the four wheels. The vehicle frame is made of a combination of Delrin and Ultimaker Tough PLA and was fabricated using an Ultimaker S5 printer. The vehicle prototype is $465mm$ long, $320.8mm$ wide, and $204.8mm$ tall. The entire system has a mass of approximately $7kg$. 1/10 Warn 8274 Winch is installed at the rear.

4.3.2 Electronics

The low-level control of the entire robot system (vehicle and manipulator) is done with an Arduino MEGA 2560 microcontroller and a U2D2 controller (shown in Figure 4.6). High-level planning is enabled by the Raspberry Pi 3B+ using ROS. The robot is powered by an 11.1V, 5000 mAh lithium-ion battery. The winch is driven by a Cytron Dual Channel 10 A DC motor driver. Each locomotive actuator is controlled using a custom

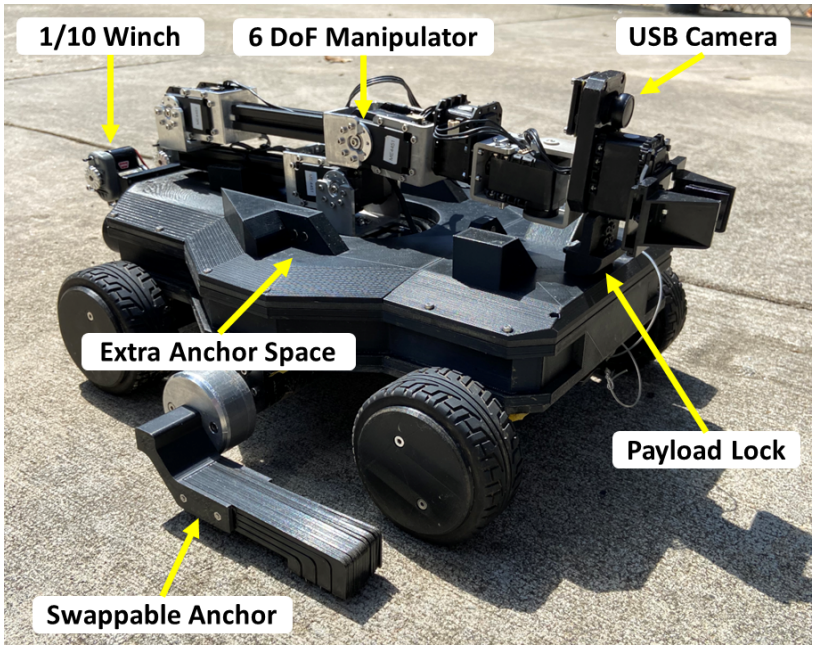

Figure 4.5: Physical prototype vehicle used in this study. A 6 DoF vehicle-mounted manipulator with a USB camera is used to localize payload, attach the payload to the vehicle, and swap anchors. The swappable anchor is used in tandem with the payload lock to pull a load using the 1/10 Warn 8274 winch installed at the rear. There is extra anchor space on top of the chassis to store a second set of anchors.

motor control board. This board takes in the encoder and hall-effect sensor data and uses a Texas Instruments DRV8871 motor driver to control the motor. Control and communications are performed with an ATMega 328p microcontroller located on each motor control board. The motor controllers communicate with the central microcontroller using I2C. This enables position and velocity control over each of the six motors.

4.3.3 Vehicle-Mounted Manipulator

This work utilizes a 6-degree-of-freedom (DoF) manipulator mounted at the center of the vehicle. The manipulator is comprised of three Dynamixel MX-106 servos, two Dynamixel MX-28 servos, and two Dynamixel AX-12A servos. A parallel-jaw gripper driven with an AX-12A servo was designed. The gripper is 3D printed and is rated for a holding force of $4.91N$. Arducam B0203 USB camera is mounted on the gripper.

The manipulator can be used for other purposes beyond swapping propulsors. This can

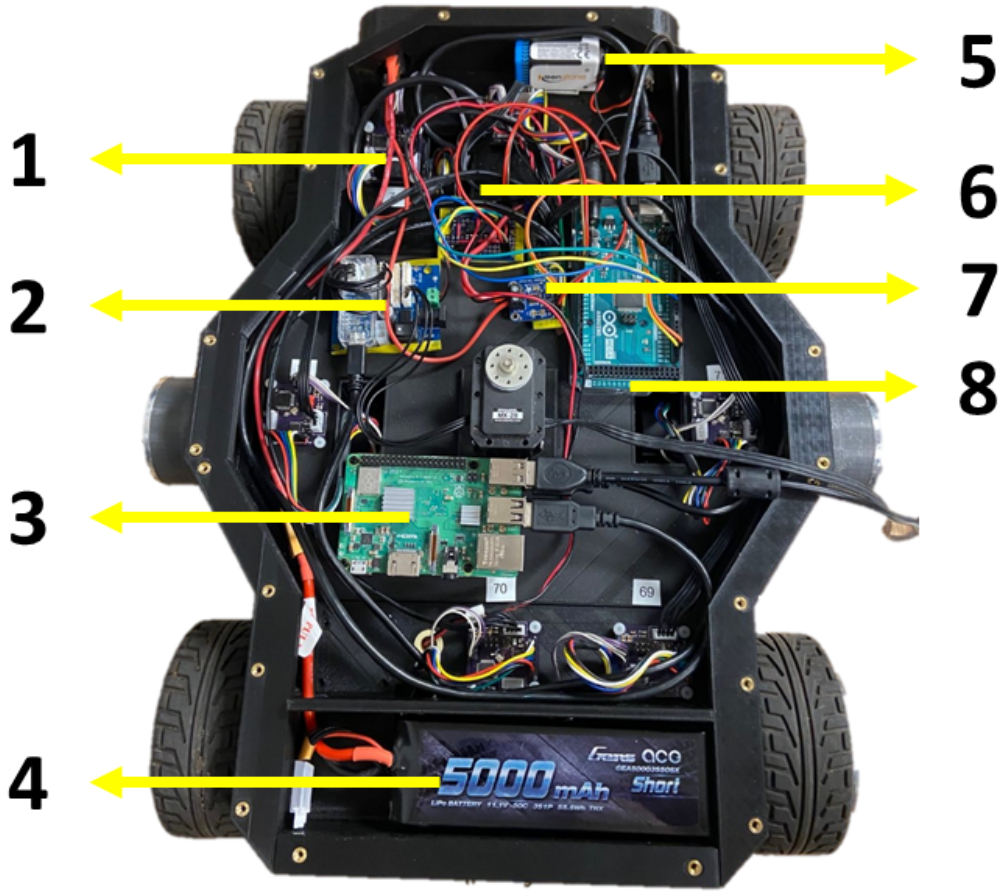

Figure 4.6: View of the internal components of the prototype vehicle. 1) Custom-built I2C motor controller board; 2) U2D2 Controller; 3) Raspberry Pi 3B+; 4) 11.1V Lithium Ion Battery; 5) 9V battery; 6) Winch Motor Controller; 7) INA260 DC Current Sensor; 8) Arduino MEGA 2560.

include sampling the environment, localizing the payload using the camera, and attaching the payload to the vehicle. The maximum payload of the manipulator is $400g$.

4.3.4 Swappable Anchors

Four different anchors are fabricated based on the surface contact designs presented in the previous section. The anchors are made of Ultimaker Tough PLA and were fabricated using an Ultimaker S5 printer.

The mounting hub on the center actuators, which house the swappable anchors, are

made of Ultimaker Tough PLA and 6061 aluminum. The T-slot mount can withstand up to $56N$. The T-slot opening is covered with a layer of $0.635mm$ thick 430 stainless steel to enable magnetic attachments.

Two $6.4mm$ nickel-plated neodymium magnets, each rated for a pull force of $5.4N$, are embedded in each anchor. If the manipulator were to detach the anchor normal to the surface, it would need to exert $9.5N$ of force. The force needed to tilt the anchor is roughly $0.2N$. Once tilted, the detachment force is greatly reduced and is roughly $0.2N$. It takes roughly $1.8N$ to slide the anchor on the surface. These forces are measured experimentally.

Microspine Anchor

Each microspine is attached to a mounting layer with a 3D printed PLA piece. The microspines are inserted mid-print at 90 to 155 degrees and then printed over. Microspines inserted at 90 to 155 degrees demonstrated maximum pull performance with a spring constant of 0.9 kN/m for a single layer. $\#10$ carbon steel fish hooks are cut in shape to be used as microspines. A pair of anchors consist of 28 layers with a total of 112 microspines.

Macrospine Anchor

Each suspension layer is embedded with $15mm$ stainless steel US standard pyramid spikes. The macrospine anchor consists of a total of 8 spikes.

Adhesive-Rubber Anchor

Each anchor mount is attached with a $101.6mm$ x $25.4mm$ x $12.7mm$ abrasion-resistant polyurethane rubber rated at 70 Durometer.

Sand Anchor

The sand anchor uses $90mm$ x $90mm$ x $10mm$ Delrin plates to provide an insertion depth of $90mm$.

4.3.5 Enabling Autonomous Payload Transport

A critical use case for the vehicle-mounted manipulator is to allow for the autonomous retrieval of target payloads. With a camera-equipped 6 DoF arm, the robot is able to scan its surrounding environment and identify target payloads using fiducial markers. The robot can then approach the payload and attach a magnetic payload lock that allows the winch to pull the load securely.

High-level motion planning, trajectory execution, and actuation of the manipulator are run on ROS using the onboard Raspberry Pi. Tracking of fiducial markers is achieved with the open-source AR-tag tracking library Alvar. The robot performs basic localization by calculating the Euclidean distance to marker reference frames and navigates toward the payload with a simple motion controller. Using the reference frame of the AR tag, the system determines the desired end-effector orientation for proper lock placement and plans a motion path using the default optimization of minimal path length. These manipulation tasks are performed through the MoveIt motion planning framework and using the Open Motion Planning Library (OMPL) planner. Once the payload lock is securely attached, the robot proceeds with transporting the payload using the winch and anchoring system. The state-machine of our planning scheme can be seen in Figure 4.7. The full demonstration of the autonomous payload transport capability is shown in Figure 4.8 and the accompanying video [45].

4.4 Performance

4.4.1 Increasing Friction to Transport Heavy Payloads

Outdoor testing was performed on surfaces readily available on Georgia Tech main campus. A series of experiments were performed to quantify and compare the performance of our prototype's maximum innate capability (without anchors) to pull payloads to the maximum payload capacity with swappable anchors. The experiments are shown in the accompanying

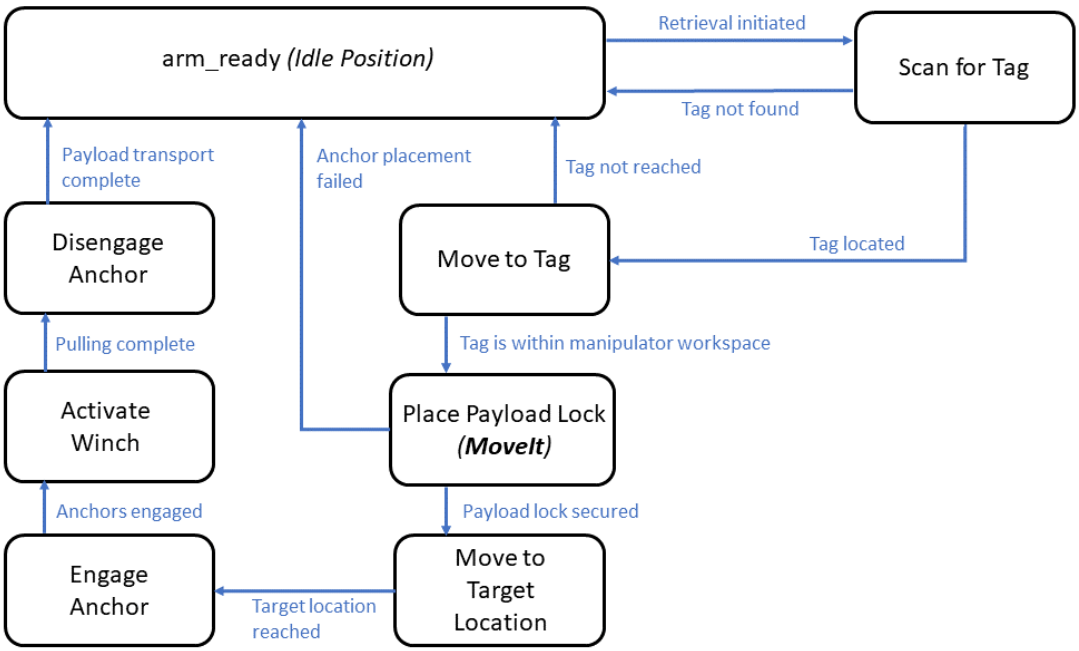

Figure 4.7: ROS high-level planner state-machine chart used to demonstrate autonomous payload attachment and transport in this study.

video [45] and in Figure 4.10.

First, to quantify the innate capability to pull payloads on different surfaces, we conducted a series of static friction tests by attaching a precision spring force gauge to our prototype vehicle. We define a vehicle's maximum innate traction to be the point at which the vehicle slips during a wheels-locked condition. For our system, the wheels are locked using position control on the drive motors. Our initial tests measured the resistive force at the onset of displacement. The tests measured the forces on five different surfaces (concrete, polysynthetic ice, sand, mud, and grass) by pulling with the spring force gauge. Once the vehicle was displaced, the experiment was stopped. The peak force was verified via video analysis and recorded for a set of different surfaces. Each surface was tested with 20 trials. With the resistive force measurements, we obtained the normalized coefficient of friction of each condition on each surface. The results can be seen in Subfigure 4.9(a).

Results from Subfigure 4.9(a) indicate that innate vehicle traction using locked wheels is consistent on concrete, mud, and grass with an averaged normalized coefficient of fric-

(a) Survey Environment and Localize Payload

(b) Approach Payload

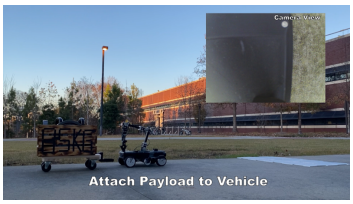

(c) Grasp Payload Lock

(d) Attach Payload to Vehicle

(e) Deploy Anchors and Pull Payload

(f) Disengage Anchors

Figure 4.8: Photographic illustration of the autonomous payload transport. (a) The robot localizes the fiducial marker on the designated payload. (b) The fiducial marker provides the relative position, and the system is then able to approach the payload. (c) The robot uses the manipulator to grasp the payload lock. (d) The robot plans a trajectory to attach the payload to the vehicle using marker frames. (e) The robot retreats and deploys the anchors onto the ground to displace the payload using the winch. (f) Lastly, the anchors are disengaged.

tion of approximately 1.06. However, on surfaces with a lower coefficient of friction such as polysynthetic ice and sand, vehicle traction degrades drastically. This clearly illustrates the need for various surface contact solutions to increase vehicle traction during payload pull. We conducted further experiments using microspine, macrospine, adhesive-rubber, and sand anchors on 5 different surfaces. These conditions did not involve using motor position control. The results are shown in Subfigure 4.9(b), Subfigure 4.9(c), Subfigure 4.9(d), and Subfigure 4.9(e) respectively.

Compared to the vehicle's innate traction, the microspine anchors demonstrated up to twice as much resistive force on concrete and grass with an increased coefficient of friction of 1.42 and 2.02 respectively. On polysynthetic ice, sand, and mud, the microspine anchors did not show much improvement.

Macrospine anchors resisted more load on mud and sand with an increased coefficient

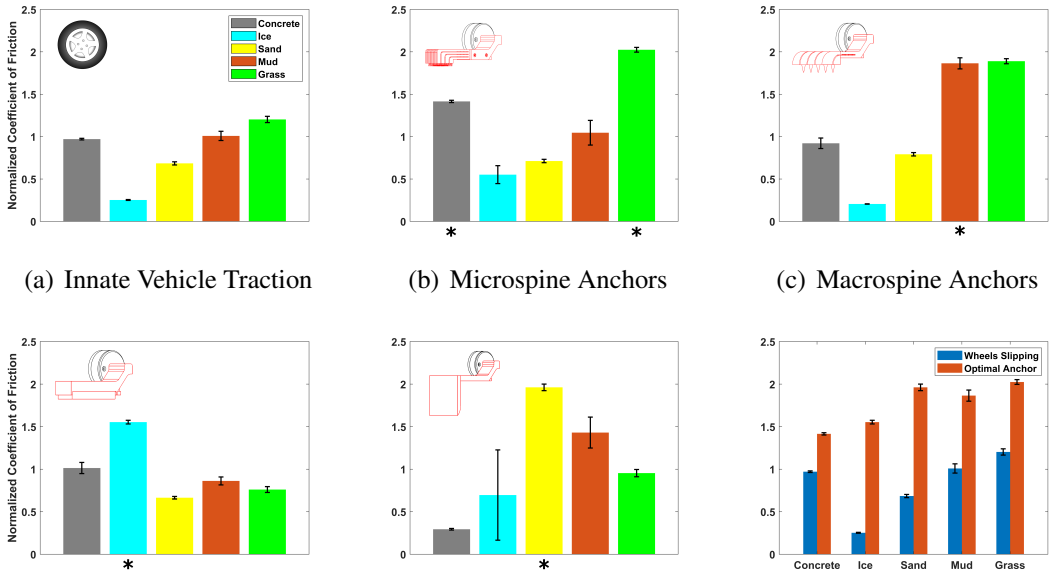

(a) Innate Vehicle Traction (b) Microspine Anchors (c) Macrospine Anchors

(d) Adhesive-Rubber Anchors (e) Sand Anchors (f) Innate Traction vs. Optimal Anchors

Figure 4.9: Bar plots showing the normalized coefficient of friction of each condition on 5 different surfaces. The optimal surface for each anchor is marked with an asterisk below. (a) Normalized coefficient of friction values using the vehicle's innate traction. (b) Normalized coefficient of friction values using microspine anchors. (c) Normalized coefficient of friction values using macrospine anchors. (d) Normalized coefficient of friction values using adhesive-rubber anchors. (e) Normalized coefficient of friction values using sand anchors. (f) Normalized coefficient of friction values comparing vehicle's innate traction vs. optimal anchors.

of friction of 1.87 and 1.89. The adhesive-rubber anchors were able to withstand six times more load on polysynthetic ice with a normalized coefficient of friction of 1.55.

Sand anchors showed three times more resistive capability on sand with an increased coefficient of friction of 1.96. These results illustrate how each anchoring device improves vehicle traction on its intended surface.

Subfigure 4.9(f) compares the vehicle's innate pulling capability to an optimal anchor's capability. Note that no single design provides excellent performance across the terrain. However, by swapping anchors, a system can improve its overall payload capacity by using an optimal anchoring solution.

We also evaluated the overall performance of the optimized swappable anchors inte-

grated with our system. Our tests consisted of measuring the maximum payload mass quantity that the vehicle could pull using the winch before the wheels began to slip. For consistency, the same surfaces were used, and the payload was placed on a wheeled cart. Maximum payload testing was conducted by placing a known weight on the cart and then having the winch pull the payload. The payload mass was increased by 5kg until the anchors failed. For this and subsequent tests, failure was defined as the robot rover displacing a full body length. The results are shown in Table 4.1.

The fully integrated system (7kg mass) was able to pull 38 times the body mass on concrete, 28 times on ice, 8 times on sand, and 16 times on mud and grass.

Table 4.1: Maximum Payload Capacity with Optimized Swappable Anchors

Concrete	**Ice**	**Sand**	**Mud**	**Grass**
265kg	195kg	60kg	115kg	115kg

Figure 4.10: Terrain testing across multiple surfaces. (1) Microspine anchors pulling up to $265kg$ on concrete. (2) Microspine anchors pulling up to $115kg$ on grass. (3) Macrospine Anchors pulling up to $115kg$ on mud. (4) Adhesive-rubber anchor pulling up to $195kg$ on polysynthetic ice. Sand Anchors pulling up to $60kg$ are shown in Figure 4.1.

4.4.2 Using Manipulation to Increase Payload Capacity Across Various Surfaces

The last step is to validate and demonstrate the actual physical adaptation. OMPL planner with optimization of minimal path length and self-collision constraints was used to demonstrate the swapping of the anchors. The trajectory planner was given specific Cartesian waypoints to execute the slide and tilt motion needed to attach/detach the anchors from the mounting hubs. The anchors were designed with handles that could mate with the gripper for consistent grasping at a fixed orientation. Closed-loop position control of the propulsor mounts is used to make sure they are aligned correctly. The entire swapping process takes $100s$. The demonstration of swapping two sets of anchors is illustrated in the accompanying video [45].

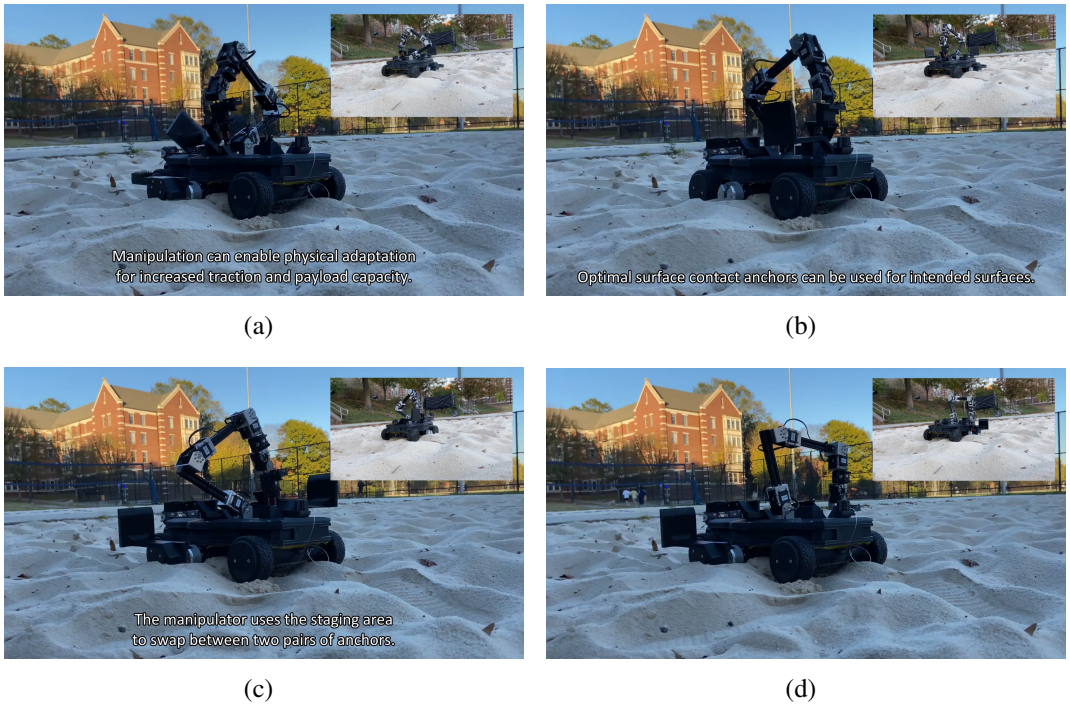

Figure 4.11: Photographic illustration of the manipulation process of swapping two anchors. (a) The manipulator relocates the right stored anchor to the staging area for swap. (b) The anchor installed on the actuator is detached and stored on the chassis. The anchor placed on the staging area is attached to the actuator for usage. (c) The manipulator swaps the right side anchors. (d) The process is repeated on the right side.

CHAPTER 5
CONCLUSION

5.1 Contributions

5.1.1 Manipulation for Efficient and Versatile Mobility

This work examined a new approach to terrestrial locomotion that leverages manipulation-driven adaptation. Specifically, this paper illustrated how a vehicle-mounted manipulator can be used to physically adjust the system for improved efficiency and versatility. The core contributions of this work are 1) developing a new manipulation-based methodology for physical adaptation, 2) creating a permanent-magnet-based mechanical design for swappable propulsors, 3) obtaining experimental results that demonstrate how swapping to wheels improves energy efficiency and swapping to legs increases versatility. This work further highlights the advantages of the swappable propulsor framework by investigating the wheel-wheg hybrid locomotion configuration. This configuration reduces the number of propulsors that need to be swapped down to a pair, decreasing the amount of time and power consumed during the process by 33%. Furthermore, the propulsors are modified to be complementary, meaning the propulsors are only actuated to overcome a unique obstacle while maintaining the energy efficiency of 4-wheeled locomotion. This work also investigates how a robotic system can use its manipulator to shift its COM to overcome a critical height.

One of the key advantages of this framework is the endless possibilities of modifications the system can undergo to overcome unique obstacles. Two unique propulsors for slippery and granular surfaces are designed and validated for usage.

5.1.2 Manipulation for Increased Payload Capacity and Versatility

In this work, we presented a mobile robotic system that utilizes a vehicle-mounted, multi-purpose manipulator to physically adapt the robot with unique anchors suitable for a particular terrain to increase payload capacity. This work presented "swappable anchors", which can be easily attached/detached to adapt the vehicle using permanent magnets. Four unique anchor designs were introduced and experimentally evaluated on five different surfaces. The experimental results illustrated how this approach can increase the overall payload capacity of a system on various surfaces by increasing the overall effective coefficient of friction. This study also experimentally demonstrated how we can use the manipulator to autonomously localize the payload using a visual sensor, attach the payload to the vehicle using a permanent-magnet-based payload key/lock, and pull several times its body mass using the swappable anchors. The proposed methods can enable ground robots to be more adaptive, robust, and autonomous. Instead of requiring redesign, the robotic system can modify itself relatively quickly and handle new terrain or conditions.

5.2 Discussion/Future Work

In this study, while the legged mode did provide greater versatility, it was not immune to failures. Specific failure modes were legs being pulled out of the T-slot and the legs breaking. The legs getting pulled out occurred mainly on forest terrain where the leg could sink into the leafy ground. This can be improved by increasing attachment force, but this has the trade-off of making desired detachment more difficult to achieve.

The 6-legged swappable propulsor gait was not optimized for maximum efficiency in this study. Optimizing the gait will make this versatile locomotion capability more efficient and reduce the overall COT across various surfaces.

Another potential failure mode is dirt/mud restricting the swappable propulsors. Permanent magnets can attach to the steel surface even with dirt/sand piling up on the steel

surface mount. However, when external debris gets caught in between the T-slot mechanism, this prevents the installation of the swappable propulsor. Over a long duration of experiments, dirt and external debris piled up within the mechanically constraining steel surface mounts. Piled-up debris within the T-slot mechanism would hinder the position of propulsors, cause detachment of propulsors, or prevent attachment of propulsors. In most cases, rotating the wheels at maximum speed in wheel mode for some time cleared the debris. For real-world deployment, a self-mitigating mechanism would need to be employed in the system. A potential solution would be to add a locking mechanism to the T-slots to prevent debris from piling up. Other solutions could include implementing a pneumatic system on the gripper to blow away the debris.

To improve the manipulation process, high-level feedback through sensors is necessary to confirm swapping and mitigate failures. One potential solution is integrating a piezo-resistive/electric pressure matrix sensor on the gripper to detect whether the swappable propulsor is grasped in the correct orientation. Combining this approach with other feedback, such as a hall-effect sensor on the surface mounts or a camera mounted on the manipulator, can ensure that the propulsors are correctly inserted for usage. These measures can prevent common failures such as dropping or misalignment of the propulsors during attachment to the mounts.

Future directions of this work involve integrating the physical adaptation capability into autonomous systems. In unknown environments, terrain and surface classifiers need to be fused to determine the most suitable propulsors or anchors for optimal performance. Swappable propulsors and anchors are designed for specific obstacles or surfaces, but it would be interesting to allow autonomous systems to experiment with different options and independently determine the most effective ones through reinforcement learning.

REFERENCES

[1] D. F. Hougen *et al.*, "A miniature robotic system for reconnaissance and surveillance," in *Proceedings 2000 ICRA. Millennium Conference. IEEE International Conference on Robotics and Automation. Symposia Proceedings (Cat. No. 00CH37065)*, IEEE, vol. 1, 2000, pp. 501–507.

[2] F. Matsuno and S. Tadokoro, "Rescue robots and systems in japan," in *2004 IEEE International Conference on Robotics and Biomimetics*, IEEE, 2004, pp. 12–20.

[3] B. M. Yamauchi, "Packbot: A versatile platform for military robotics," in *Unmanned ground vehicle technology VI*, International Society for Optics and Photonics, vol. 5422, 2004, pp. 228–237.

[4] R. D. Quinn, J. T. Offi, D. A. Kingsley, and R. E. Ritzmann, "Improved mobility through abstracted biological principles," in *IEEE/RSJ International Conference on Intelligent Robots and Systems*, IEEE, vol. 3, 2002, pp. 2652–2657.

[5] S. Kim and P. M. Wensing, "Design of dynamic legged robots," *Foundations and Trends in Robotics*, vol. 5, no. 2, pp. 117–190, 2017.

[6] M. Arai, Y. Tanaka, S. Hirose, H. Kuwahara, and S. Tsukui, "Development of "souryu-iv" and "souryu-v:" serially connected crawler vehicles for in-rubble searching operations," *Journal of Field Robotics*, vol. 25, no. 1-2, pp. 31–65, 2008.

[7] A. Schiele *et al.*, "Nanokhod exploration rover-a rugged rover suited for small, low-cost, planetary lander mission," *IEEE robotics & automation magazine*, vol. 15, no. 2, pp. 96–107, 2008.

[8] U. Saranli, M. Buehler, and D. E. Koditschek, "Rhex: A simple and highly mobile hexapod robot," *The International Journal of Robotics Research*, vol. 20, no. 7, pp. 616–631, 2001.

[9] J. M. Morrey, B. Lambrecht, A. D. Horchler, R. E. Ritzmann, and R. D. Quinn, "Highly mobile and robust small quadruped robots," in *Proceedings 2003 IEEE/RSJ International Conference on Intelligent Robots and Systems (IROS 2003)(Cat. No. 03CH37453)*, IEEE, vol. 1, 2003, pp. 82–87.

[10] Y.-S. Kim, G.-P. Jung, H. Kim, K.-J. Cho, and C.-N. Chu, "Wheel transformer: A miniaturized terrain adaptive robot with passively transformed wheels," in *2013 IEEE International Conference on Robotics and Automation*, IEEE, 2013, pp. 5625–5630.

[11] Y. She, C. J. Hurd, and H.-J. Su, "A transformable wheel robot with a passive leg," in *2015 IEEE/RSJ International Conference on Intelligent Robots and Systems (IROS)*, IEEE, 2015, pp. 4165–4170.

[12] A. T. Asbeck, S. Kim, M. R. Cutkosky, W. R. Provancher, and M. Lanzetta, "Scaling hard vertical surfaces with compliant microspine arrays," *The International Journal of Robotics Research*, vol. 25, no. 12, pp. 1165–1179, 2006.

[13] A. Parness, N. Abcouwer, C. Fuller, N. Wiltsie, J. Nash, and B. Kennedy, "Lemur 3: A limbed climbing robot for extreme terrain mobility in space," in *2017 IEEE International Conference on Robotics and Automation (ICRA)*, IEEE, 2017, pp. 5467–5473.

[14] J. Park, D. H. Kong, and H.-W. Park, "Design of anti-skid foot with passive slip detection mechanism for conditional utilization of heterogeneous foot pads," *IEEE Robotics and Automation Letters*, vol. 4, no. 2, pp. 1170–1177, 2019.

[15] A. Foris, N. Wagener, B. Boots, and A. Mazumdar, "Exploiting singular configurations for controllable, low-power friction enhancement on unmanned ground vehicles," *IEEE Robotics and Automation Letters*, vol. 5, no. 2, pp. 3556–3563, 2020.

[16] J. B. Jeans and D. Hong, "Impass: Intelligent mobility platform with active spoke system," in *2009 IEEE International Conference on Robotics and Automation*, IEEE, 2009, pp. 1605–1606.

[17] S.-C. Chen, K.-J. Huang, W.-H. Chen, S.-Y. Shen, C.-H. Li, and P.-C. Lin, "Quattroped: A leg–wheel transformable robot," *IEEE/ASME Transactions On Mechatronics*, vol. 19, no. 2, pp. 730–742, 2013.

[18] W.-H. Chen, H.-S. Lin, Y.-M. Lin, and P.-C. Lin, "Turboquad: A novel leg–wheel transformable robot with smooth and fast behavioral transitions," *IEEE Transactions on Robotics*, vol. 33, no. 5, pp. 1025–1040, 2017.

[19] J. E. Clark *et al.*, "Biomimetic design and fabrication of a hexapedal running robot," in *Proceedings 2001 ICRA. IEEE International Conference on Robotics and Automation (Cat. No. 01CH37164)*, IEEE, vol. 4, 2001, pp. 3643–3649.

[20] J. E. Bares and D. S. Wettergreen, "Dante ii: Technical description, results, and lessons learned," *The International Journal of robotics research*, vol. 18, no. 7, pp. 621–649, 1999.

[21] M. Hutter *et al.*, "Anymal-a highly mobile and dynamic quadrupedal robot," in *2016 IEEE/RSJ International Conference on Intelligent Robots and Systems (IROS)*, IEEE, 2016, pp. 38–44.

[22] F. Rubio, F. Valero, and C. Llopis-Albert, "A review of mobile robots: Concepts, methods, theoretical framework, and applications," *International Journal of Advanced Robotic Systems*, vol. 16, no. 2, p. 1 729 881 419 839 596, 2019.

[23] D. L. Christensen, E. W. Hawkes, S. A. Suresh, K. Ladenheim, and M. R. Cutkosky, "μTugs: Enabling microrobots to deliver macro forces with controllable adhesives," in *2015 IEEE International Conference on Robotics and Automation (ICRA)*, IEEE, 2015, pp. 4048–4055.

[24] M. P. Murphy, C. Kute, Y. Mengüç, and M. Sitti, "Waalbot ii: Adhesion recovery and improved performance of a climbing robot using fibrillar adhesives," *The International Journal of Robotics Research*, vol. 30, no. 1, pp. 118–133, 2011.

[25] E. W. Hawkes, D. L. Christensen, and M. R. Cutkosky, "Vertical dry adhesive climbing with a 100× bodyweight payload," in *2015 IEEE International Conference on Robotics and Automation (ICRA)*, IEEE, 2015, pp. 3762–3769.

[26] J. Xiao, B. Li, K. Ushiroda, and Q. Song, "Rise-rover: A wall-climbing robot with high reliability and load-carrying capacity," in *2015 IEEE International Conference on Robotics and Biomimetics (ROBIO)*, IEEE, 2015, pp. 2072–2077.

[27] K. Carpenter, N. Wiltsie, and A. Parness, "Rotary microspine rough surface mobility," *IEEE/ASME Transactions on Mechatronics*, vol. 21, no. 5, pp. 2378–2390, 2015.

[28] W. Ruotolo, F. S. Roig, and M. R. Cutkosky, "Load-sharing in soft and spiny paws for a large climbing robot," *IEEE Robotics and Automation Letters*, vol. 4, no. 2, pp. 1439–1446, 2019.

[29] S. Wang, H. Jiang, and M. R. Cutkosky, "A palm for a rock climbing robot based on dense arrays of micro-spines," in *2016 IEEE/RSJ International Conference on Intelligent Robots and Systems (IROS)*, IEEE, 2016, pp. 52–59.

[30] M. J. Spenko *et al.*, "Biologically inspired climbing with a hexapedal robot," *Journal of field robotics*, vol. 25, no. 4-5, pp. 223–242, 2008.

[31] A. Parness, "Anchoring foot mechanisms for sampling and mobility in microgravity," in *2011 IEEE International Conference on Robotics and Automation*, IEEE, 2011, pp. 6596–6599.

[32] A. Parness, M. Frost, N. Thatte, and J. P. King, "Gravity-independent mobility and drilling on natural rock using microspines," in *2012 IEEE International Conference on Robotics and Automation*, IEEE, 2012, pp. 3437–3442.

[33] J. S. Lee and R. S. Fearing, "Anisotropic collapsible leg spines for increased millirobot traction," in *2015 IEEE International Conference on Robotics and Automation (ICRA)*, IEEE, 2015, pp. 4547–4553.

[34] J. S. Lee, *Increased millirobot traction in running and jumping through leg spines*. University of California, Berkeley, 2018.

[35] M. A. Estrada, S. Mintchev, D. L. Christensen, M. R. Cutkosky, and D. Floreano, "Forceful manipulation with micro air vehicles," *Science Robotics*, vol. 3, no. 23, 2018.

[36] A. L. Desbiens, A. Asbeck, and M. Cutkosky, "Hybrid aerial and scansorial robotics," in *2010 IEEE International Conference on Robotics and Automation*, IEEE, 2010, pp. 72–77.

[37] J. Fernandez and A. Mazumdar, "Tail-based anchoring on granular media for transporting heavy payloads," *IEEE Robotics and Automation Letters*, vol. 6, no. 2, pp. 1232–1239, 2021.

[38] C. C. Berdan, B. G. Johnson, and E. W. Hawkes, "Microspine-rubber composite for high friction on smooth, rough, and wet surfaces," in *2021 IEEE/RSJ International Conference on Intelligent Robots and Systems (IROS)*, IEEE, 2021, pp. 7384–7390.

[39] A. D. Marchese, H. Asada, and D. Rus, "Controlling the locomotion of a separated inner robot from an outer robot using electropermanent magnets," in *2012 IEEE International Conference on Robotics and Automation*, 2012, pp. 3763–3770.

[40] S. Hirose, M. Imazato, Y. Kudo, and Y. Umetani, "Internally-balanced magnet unit," *Advanced Robotics*, vol. 1, no. 3, pp. 225–242, 1986.

[41] A. Mazumdar and H. H. Asada, "Mag-foot: A steel bridge inspection robot," in *2009 IEEE/RSJ International Conference on Intelligent Robots and Systems*, IEEE, 2009, pp. 1691–1696.

[42] R. Kim, A. Debate, S. Balakirsky, and A. Mazumdar, "Using manipulation to enable adaptive ground mobility," in *2020 IEEE International Conference on Robotics and Automation (ICRA)*, 2020, pp. 857–863.

[43] J. D. Weingarten, M. Buehler, R. E. Groff, and D. E. Koditschek, "Gait generation and optimization for legged robots," in *The IEEE International Conference on Robotics and Automation*, 2002.

[44] V. Tucker, "The energetic cost of moving about," *American Scientist*, vol. 63, no. 4, pp. 413–419, 1975.

[45] R. Kim, E. Diller, E. Harkonen, and A. Mazumdar, *Increasing mobile robot payload capacity through multipurpose manipulation*, https://youtu.be/0chaPN2KOwA, Accessed: 2022/12/16.

[46] D. Stowe, K. Conger, J. D. Summers, P. Joseph, B. Thompson, and J. Matthews, "Designing a lunar wheel," in *International Design Engineering Technical Conferences and Computers and Information in Engineering Conference*, vol. 43291, 2008, pp. 627–639.

[47] R. D. Lorenz, J. R. Zimbelman, R. D. Lorenz, and J. R. Zimbelman, "Moving on sand," *Dune Worlds: How Windblown Sand Shapes Planetary Landscapes*, pp. 259–272, 2014.

[48] R. B. Foltz, "Sediment reduction from the use of lowered tire pressures," *SAE transactions*, pp. 376–381, 1994.

[49] P. Abad-Manterola, J. W. Burdick, I. A. Nesnas, S. Chinchali, C. Fuller, and X. Zhou, "Axel rover paddle wheel design, efficiency, and sinkage on deformable terrain," in *2010 IEEE International Conference on Robotics and Automation*, IEEE, 2010, pp. 2821–2827.

[50] R. Kim, A. Debate, S. Balakirsky, and A. Mazumdar, "Using manipulation to enable adaptive ground mobility," in *2020 IEEE International Conference on Robotics and Automation (ICRA)*, IEEE, 2020, pp. 857–863.

[51] R. Kim, V. Madabushi, E. Dong, and A. Mazumdar, "Increasing mobile robot efficiency and versatility through manipulation-driven adaptation," *Journal of Mechanisms and Robotics*, vol. 13, no. 5, p. 050 906, 2021.

[52] M. Martone, C. Pavlov, A. Zeloof, V. Bahl, and A. M. Johnson, "Enhancing the vertical mobility of a robot hexapod using microspines," *arXiv preprint arXiv:1906.04811*, 2019.

[53] S. Godon, A. Ristolainen, and M. Kruusmaa, "An insight on mud behavior upon stepping," *IEEE Robotics and Automation Letters*, vol. 7, no. 4, pp. 11 039–11 046, 2022.

[54] J. Y. Wong, *Terramechanics and off-road vehicle engineering: terrain behaviour, off-road vehicle performance and design*. Butterworth-heinemann, 2009.

VITA

Raymond Sunghwan Kim was born on October 9, 1994, in Austin, Texas. He graduated from Taejon Christian International School in 2013 before attending Rice University. He graduated in 2017 with a Bachelor's Degree in Mechanical Engineering and enrolled in the Robotics Ph.D. Program at the Georgia Institute of Technology. His research interests include testing and pushing the physical limits of robots and creating novel and intelligent solutions to overcome them.